This document is confidential and is proprietary to the American Chemical Society and its authors. Do not copy or disclose without written permission. If you have received this item in error, notify the sender and delete all copies.

Composition–Structure–Solubility Relationships in Borosilicate Glasses: Towards a Rational Design of Bioactive Glasses with Controlled Dissolution Behavior

Journal:	*ACS Applied Materials & Interfaces*
Manuscript ID	am-2021-07519x.R1
Manuscript Type:	Article
Date Submitted by the Author:	06-Jun-2021
Complete List of Authors:	Stone-Weiss, Nicholas; Rutgers The State University of New Jersey, Materials Science and Engineering Bradtmüller, Henrik; Westfalische Wilhelms-Universitat Munster Institut fur Physikalische Chemie; Federal University of Sao Carlos, Department of Materials Engineering Eckert, Hellmut; University of Sao Paulo Institute of Physics of Sao Carlos; Westfalische Wilhelms-Universitat Munster Institut fur Physikalische Chemie Goel, Ashutosh; Rutgers The State University of New Jersey, Materials Science and Engineering

SCHOLARONE™
Manuscripts

Composition–Structure–Solubility Relationships in Borosilicate Glasses: Towards a Rational Design of Bioactive Glasses with Controlled Dissolution Behavior

Nicholas Stone-Weiss,[1] Henrik Bradtmüller,[2,3] Hellmut Eckert,[2,4] Ashutosh Goel[1,1]

[1]Department of Materials Science and Engineering, Rutgers, The State University of New Jersey, Piscataway, NJ 08854, United States

[2]Institut für Physikalische Chemie, WWU Münster, Corrensstrasse 30, D48149 Münster, Germany

[3]Federal University of São Carlos, Department of Materials Engineering, CP 676, 13565-905 São Carlos, SP, Brazil

[4]São Carlos Institute of Physics, University of São Paulo, Avenida Trabalhador Saocarlense 400, São Carlos, SP 13566-590, Brazil

[1] Corresponding author:
Email: ag1179@soe.rutgers.edu; Ph: +1-848-333-1523

Abstract

Owing to their fast but tunable degradation kinetics (in comparison to silicates) and excellent bioactivity, the past decade has witnessed an upsurge in the research interest of borate/borosilicate-based bioactive glasses for their potential use in a wide range of soft tissue regeneration applications. Nevertheless, most of these glasses have been developed using trial-and-error approaches wherein SiO_2 has been gradually replaced by B_2O_3. One major reason for using this empirical approach is the complex short-to-intermediate range structures of these glasses which greatly complicate the development of a thorough understanding of composition–structure–solubility relationships in these systems. Transitioning beyond the current style of composition design to a style that facilitates the development of bioactive glasses with controlled ion release tailored for specific patients/diseases requires a deeper understanding of the compositional/structural dependence of glass degradation behavior *in vitro* and *in vivo*. Accordingly, the present study aims to decipher the structural drivers controlling the dissolution kinetics and ion-release behavior of potentially bioactive glasses designed in the Na_2O–B_2O_3–P_2O_5–SiO_2 system across a broad compositional space in simulated body environments (pH = 7.4). By employing *state-of-the-art* spectroscopy-based characterization techniques, it has been shown that the degradation kinetics of borosilicate glasses depend on their *R* (Na/B) and *K* (Si/B) ratios, while the release of particular network forming moieties from the glass into solution is strongly influenced by their role in – and effect on – the short-to-intermediate-range molecular structure. The current study aims to promote a rational design of borosilicate-based bioactive glasses, where a delicate balance between maximizing soft tissue regeneration and minimizing calcification and cytotoxicity can be achieved by tuning the release of ionic dissolution products (of controlled identity and abundance) from bioactive glasses into physiological media.

Keywords

Bioactive glass, Compositional design, Dissolution, Solid-state NMR

1. Introduction

The last 5+ years have witnessed a noticeable upsurge in the research interest of borate- and borosilicate-based bioactive glasses for use in soft tissue engineering, given their ability to degrade (*i.e.*, release functional ions and resorb over time) at a controlled pace, thus promoting biological processes such as antibacterial activity and angiogenesis.[1-4] For instance, fibrous borate-based bioactive glass (13-93B3), Dermafuse®/MIRRAGEN® Advanced Wound Matrix, was initially approved for use in healing open wounds in animals. Nevertheless, these materials have recently been approved for treating acute or chronic wounds in human patients.[1] While these developments are tremendous for the field of soft tissue engineering, ongoing research indicates that these advances merely represent the 'tip of the iceberg' as compared to the full therapeutic scope of boron-containing bioactive glasses.[4, 5] This is particularly evidenced by the finding that borate-based glasses are not only successful in promoting accelerated vascular regeneration *in vivo*, they also exhibit non-cytotoxic behavior when in contact with kidney tissue.[6] Given that the kidney is considered to be the organ most prone to borate toxicity,[6] it can be inferred that similar glasses can be designed for a wide range of applications in soft-tissue engineering, with the assurance that borate release will not significantly affect cell viability.

A few emerging areas in soft tissue engineering where boron-containing bioactive glasses with controlled dissolution behavior are expected to play an important role in the future include cardiac and pulmonary tissue engineering, and muscle and nerve regeneration.[7, 8] The preliminary results on this subject report the cytocompatibility of borate and silicate glass rods/microfibers with neuronal cells, while these materials have also been successful as synthetic nerve guidance conduits for treating peripheral nerve damage, thus, promoting short-gap axon regeneration.[9-11] Further, the glass-based scaffold analogs have also been used to direct long-gap axon growth.[12-14]

Similarly, the high efficacy of aluminoborate-based glasses (with dissolution rates between commercial silicate- and borate-based bioactive glasses) in promoting the regeneration of skeletal muscle tissue *in vivo* has recently been reported.[15] The aforementioned applications of bioactive glasses in the field of soft tissue engineering (and beyond) represent the future of biomaterials. Therefore, novel glass compositions with controlled degradation kinetics are required whose dissolution behavior and functional ion release can be tailored for specific patients/diseases.

2. Challenges with the current design of silicate and borate-based bioactive glasses in the repair and regeneration of soft tissues inside the human body

The majority of silicate bioactive glasses [*e.g.*, 45S5 Bioglass® (wt.%: 45 SiO_2 – 24.5 Na_2O – 24.5 CaO – 6 P_2O_5) and S53P4 (wt.%: 53 SiO_2 – 23 CaO – 20 Na_2O – 4 P_2O_5)] are designed in the Na_2O-CaO-SiO_2 ternary system. However, the interaction of these glasses with physiological fluids usually occurs at a slow rate, thus, causing the undissolved glass to remain in the body for durations longer (months to years) than the recovery period of the tissue.[3, 16] In most cases, this slower degradation rate is undesirable for soft tissue engineering, especially when these glasses are being used for the repair and regeneration of soft tissues *in vivo*, such as in the case of cardiac or pulmonary tissue engineering. For example, bioactive glasses meant for repair and regeneration of myocardial infarcted tissue ought to be fully biodegradable, while also matching the recovery rate of the injured heart (*i.e.*, 2 weeks to 3 months in the case of an acute myocardial infarction).[17-19] In the same context, borate and phosphate bioactive glasses achieve complete (100%) degradation,[20] and, thus have been proposed for soft tissue engineering (*e.g.*, wound healing).[21, 22] However, the degradation kinetics of such glasses are too fast for application in cardiac or pulmonary tissue engineering.[23, 24] For example, bioactive glass particles (diameter: 0.2-5 μm) with

the composition 5.5 Na_2O – 11.1 K_2O – 4.6 MgO – 18.5 CaO – 3.7 P_2O_5 – 56.6 B_2O_3 (wt.%) achieve near 100% degradation after ~14 days in simulated body fluid,[25] which is significantly faster compared to the recovery rate of the injured heart.[17, 18]

Further, most commercially available bioactive glasses – *e.g.*, 45S5 Bioglass® and 13-93B3 – were originally developed for bone regeneration, wherein the mineralization of hydroxycarbonate apatite (HCA) – or calcification – is an essential trait.[16] However, severe consequences can occur if calcification occurs in regions that do not normally calcify. Critical health-related issues that could arise from calcification within such soft tissues are summarized elsewhere.[26, 27]

For calcification to initiate, a nidus for crystallization is required, along with an adequate supply of local Ca^{2+} and PO_4^{3-}.[28] It has been demonstrated that serum phosphate level (*i.e.*, the concentration of PO_4^{3-}) is an important *in vivo* determinant of calcification.[29, 30] Lowering their concentrations can reduce or avoid soft tissue calcification, even in the presence of extremely high serum calcium levels.[29, 30] Interestingly, nearly all commercial bioactive glasses are rich sources of Ca^{2+} and PO_4^{3-}. Therefore, the bioactive glasses currently available in the marketplace – on account of providing a conducive environment for calcification of the soft tissues – are largely unsuitable for applications in cardiac and pulmonary tissue engineering. Indeed, the possibility of 45S5 Bioglass® (and other bioactive glasses) to incite soft tissue calcification has been well-documented in the literature.[3, 4, 7, 8] However, our literature survey did not identify studies attempting to resolve this problem – that is, designing glasses that can stimulate soft tissue repair and regeneration while also suppressing calcification of the scaffold and tissue.

3. Borosilicate glasses as potential candidates for application in soft tissue repair and regeneration inside the human body

Borosilicate glasses provide certain advantages over standard silicate- or borate-based compositions, including (i) a broader glass-forming range, (ii) flexible and tunable short-to-intermediate structure[31-35] that allow the incorporation and controlled release of various functional ions (*e.g.*, Ag^{+}, Mg^{2+}, Sr^{2+}, Cu^{2+}, and Co^{2+}) with therapeutic abilities and suppression of calcification, in both *in vitro* and *in vivo* conditions,[36-39] (iii) tunable degradation mechanisms and rates resulting in both congruent/incongruent dissolution behavior,[40, 41] and (iv) ease of processing into porous three-dimensional scaffolds or fibers for application in tissue engineering.[1, 16] Recent studies have further shown the ability of borosilicate glasses to promote angiogenesis and tissue repair *in vivo*.[41, 42] These features make borosilicate-based bioactive glasses an attractive candidate for application in the treatment of a broad range of non-skeletal biomedical problems.

Accordingly, the present study aims to elucidate the composition – structure – solubility relationships in model borosilicate-based bioactive glasses designed in the Na_2O–B_2O_3–P_2O_5–SiO_2 system. The glasses have been designed over a broad compositional space where the baseline sodium borosilicate (P_2O_5-free) glasses have been chosen in the perboric (Na/B < 1), metaboric (Na/B = 1), and peralkaline (Na/B > 1) regimes, adding P_2O_5 in a stepwise manner. As discussed elsewhere in more detail,[35] CaO-free model glasses have been selected for this study: (i) to simplify the glass structure and mitigate competition between Ca^{2+} and Na^{+}, and (ii) to benefit from the wide glass-forming range of the studied system, allowing the study of more varied glass compositions. Also, CaO-free bioactive glasses and ceramics have been reported in the literature.[43-46]

Further, although the previous section highlights the potential adverse effects of dissolved PO_4^{3-} species in the context of soft tissue calcification, the release of phosphate species from P_2O_5-doped glasses into local environments at controlled rates is still vital in promoting several angiogenic processes.[3, 47-49] Thus, P_2O_5 (in limited concentrations) is anticipated to remain an important constituent of bioactive glasses suited for soft tissue applications.

Through a comprehensive study utilizing several *state-of-the-art* characterization techniques, including inductively coupled plasma – optical emission spectroscopy (ICP-OES) and advanced (single and double resonance) magic-angle spinning nuclear magnetic resonance (MAS NMR) spectroscopy, among others, we aim to generate a comprehensive understanding of the structural and compositional drivers controlling the ionic release behavior during glass degradation in simulated body environments. The overarching long-term goal is to establish a foundation of the fundamental knowledge required to promote a rational design of borosilicate-based bioactive glasses, where a delicate balance between maximizing soft tissue repair and regeneration and minimizing calcification and cytotoxicity can be achieved *via* tuning the release of ionic dissolution products (of controlled identity and abundance) from bioactive glasses into the physiological media.

4. Experimental

4.1 Glass compositional design and synthesis

Glasses selected for the study fall into three groups with respect to their Na_2O/B_2O_3 ratios, R, including perboric (PB, $R < 1$), metaboric (MB, $R = 1$), and peralkaline (PA, $R > 1$) compositions. Each of the three baseline glass compositions, (i) 25 Na_2O–30 B_2O_3–45 SiO_2 (R = 0.83), (ii) 25 Na_2O–25 B_2O_3–50 SiO_2 (R = 1), and (iii) 25 Na_2O–20 B_2O_3–55 SiO_2 (R = 1.25), lie

Table 1. All batched compositions of studied glasses as compared to selected experimental compositions (in brackets), as analyzed via ICP-OES (±0.5 mol. %). N_4 values (in percent) from fitted ^{11}B MAS NMR (±0.5 %), average number of B(IV) next nearest neighbors around P $<m_B(P)>$, average number of bridging oxygen atoms per phosphate and silicate unit ($<n_P>$ and $<n_{Si}>$, respectively; ±0.02), as determined in Ref. 35.

Sample ID	Batched				MAS NMR			
	Na_2O	P_2O_5	B_2O_3	SiO_2	N_4	$<m_B(P)>$	$<n_P>$	$<n_{Si}>$
PB0	25.0 [25.3]	--	30.0 [29.7]	45.0 [45.0]	63.7	--	--	3.71
PB2-P1	24.8	1.0	29.7	44.6	63.4	0.47	1.23	3.82
PB2-P3	24.3 [25.9]	3.0 [3.0]	29.1 [29.0]	43.7 [42.2]	61.8	0.65	1.45	3.85
PB2-P5	23.8 [25.8]	5.0 [5.0]	28.5 [29.1]	42.8 [40.0]	58.5	0.90	1.74	3.88
MB0	25.0 [25.1]	--	25.0 [25.0]	50.0 [49.9]	67.2	--	--	3.67
MB2-P1	24.8	1.0	24.8	49.5	67.5	0.69	1.25	3.75
MB2-P3	24.3 [26.0]	3.0 [3.0]	24.3 [23.9]	48.5 [47.1]	67.2	0.81	1.45	3.78

within the homogeneous glass-forming regions of the sodium borosilicate ternary diagram. P_2O_5 has been gradually added to the baseline compositions, resulting in the following three series of glasses (mol.%):

Series PB2-P*x*: x P_2O_5–(100-x) (25 Na_2O–30 B_2O_3–45 SiO_2) x = 0, 1, 3, 5

Series MB2-P*x*: x P_2O_5–(100-x) (25 Na_2O–25 B_2O_3–50 SiO_2) x = 0, 1, 3, 5

Series PA2-P*x*: x P_2O_5–(100-x) (25 Na_2O–20 B_2O_3–55 SiO_2) x = 0, 1, 3

The glass synthesis and annealing procedures along with their in-depth structural analysis (both experimental and computational) have been discussed elsewhere.[35] Table 1 presents the batched vs. experimental glass compositions, as analyzed on selected samples by ICP-OES (PerkinElmer Optima 7300V) for B_2O_3, P_2O_5, and SiO_2 and flame emission spectroscopy (PerkinElmer Flame Emission Analyst 200) for Na_2O. Differential scanning calorimetry (DSC) data were collected on glass powders (particle size: <45 μm diameter) using a simultaneous thermal analyzer (STA 449 F5 Jupiter®; Netzsch) from room temperature to 1400 °C (in Pt crucibles) at a heating rate of 20 °C/min under a constant flow of nitrogen gas. The experimental glass transition temperatures, T_g, were determined from the onset of the apparent change in heat capacity in the DSC curve.

MB2-P5	23.8 [24.7]	5.0 [5.0]	23.8 [23.9]	47.5 [46.3]	65.5	0.86	1.56	3.92
PA0	25.0 [25.1]	--	20.0 [20.1]	55.0 [54.8]	71.3	--	--	3.62
PA2-P1	24.8	1.0	19.8	54.5	72.2	0.67	1.24	3.68
PA2-P3	24.3 [25.1]	3.0 [3.1]	19.4 [19.3]	53.4 [52.6]	72.2	0.74	1.36	3.77

4.2 Sample preparation for chemical degradation experiments

The chemical dissolution studies were performed on glass powders in the particle size range of 300 μm – 425 μm. The details related to the preparation of glass particles followed by the methodology for the determination of their three-dimensional (3D) geometric surface area have been presented in our previous article.[40] Experimental density values (reported in our previous publication[35]) were used together with the 3D surface area calculations to determine the specific surface area of the washed powders (4200±300 mm^2/g). Finally, the mass of glass particles resulting in the desired surface area (SA) was calculated.

Based on the results of the degradation behavior of powder samples, similar tests were performed on polished monolithic glass coupons (n = 3) with dimensions ~10 mm × ~10 mm. The details about the polishing of glass coupons have been presented in our previous article.[50] The thickness of the polished samples varied between 1-2 mm. The dimensions of the rectangular polished samples were measured to calculate the geometric surface areas, SA.

4.3 Glass degradation experiments in simulated body environments

4.3.1 Degradation behavior and kinetics of glass corrosion

Glass degradation behavior and kinetics were studied in Tris-HCl and Tris-HNO_3 buffer solutions with pH = 7.4 (representing the typical physiological pH). Solutions were prepared by dissolving 13.25 g of Tris (Tris(hydroxymethyl)aminomethane; Alfa Aesar; ≥99.8%) in de-ionized water and adjusting the pH to the desired value with either 1 M HCl or 1 M HNO_3. Solutions were prepared as target pH ±0.02 in batches with a total volume of 1.00 ± 0.05 L to maintain accurate

Tris molarity in the solution. In each experiment, 60.0 mg of acetone-washed glass particles were immersed in 50.0 mL of solution, corresponding to a SA/V of 5 m^{-1}, where V is the volume of the Tris-buffer solution used. In order to calculate the SA of the powder added to the experiments, the specific surface areas of the glasses (calculated using a 3D geometric approximation) were utilized as a conversion factor from mass to surface area. All powder–solution mixtures were immediately sealed into sterilized polypropylene flasks and placed in an oven at 37±1 ºC. Solution preparation and experimental conditions followed ISO 10993-14,[51] complemented by the crucial substitution of HNO_3 in place of HCl as the acid utilized in Tris-based solutions. The selection of HNO_3 over HCl was made based on our previous studies[52] and relevant literature on this topic. For example, Tournié et al.[53] have shown that the degradation kinetics of borosilicate glasses (in the forward rate regime) accelerates by a factor of ~2 in Tris-HCl as compared to Tris-HNO_3. Although Tris-HNO_3 based solutions were utilized for experiments on series PB2-P*x* and PA2-P*x* glasses, comparative experiments with both Tris-HCl and Tris-HNO_3 based solutions were performed on the MB2-P*x* glass series.

The duration of degradation experiments varied between 1 hour and 28 days. Besides analyses of neat (unused) and blank (glass-free) control solutions, all experiments were performed in triplicate to capture the experimental uncertainty. The pH of each solution recovered from experiments was measured at room temperature using a pH meter (Mettler Toledo InLab® Pro-ISM). Separate aliquots of recovered solutions were chemically analyzed by ICP-OES (PerkinElmer Optima 8300). ICP-OES detection limits were <0.5 ppm for Na and P and <0.2 ppm for B and Si. The normalized loss (NL) of each element (Na, B, P, and Si) released from the glass into the surrounding solution was calculated using equation (1),

$$NL_i = \frac{C_i - C_o}{\left(\frac{SA}{V}\right) f_i} \qquad (1)$$

where C_i is the mass concentration of element i in the solution as detected by ICP-OES; f_i is the mass fraction of the element i in the glass, and C_o is the background concentration (as determined from blank solutions). Normalized loss data, specified in units of mol/m^2 were plotted against time and linearly fit over the apparent linear regimes of release at early times to evaluate forward dissolution rates for each glass composition.

4.3.2 Structural evolution of the glass powders due to degradation

To study the kinetics and mechanisms of glass degradation in buffer solutions, bulk and surface characterization were performed on both pre- and post-degradation glass specimens. The glass powders remaining after the degradation experiments *(from section 4.3.1)* were rinsed thrice in deionized (DI) water, followed by rinsing in ethanol (Fisher Chemical, anhydrous) to remove any water adhering to the surface of glass particles. The powders were then dried at room temperature in an ambient atmosphere and analyzed by X-ray diffraction (XRD; PANalytical – X'Pert Pro; Cu K_α radiation; 2θ range: 10–90º; step size: 0.01313º s^{-1}) to confirm the presence/absence of any secondary crystalline phases.

Further, the recovered glass powders were additionally analyzed using FTIR spectroscopy (FTIR-UATR, Frontier™, PerkinElmer, Inc.; scanning resolution 4 cm^{-1}, 32 scans for background and samples) and single resonance ^{11}B, ^{31}P, and ^{29}Si MAS NMR spectroscopy to assess the structural changes occurring as a result of degradation processes. The parameters used in single resonance MAS NMR experiments of post-degradation samples have been summarized in Table 2. The NMR spectra were analyzed using the DMFit software,[54] utilizing Gauss/Lorentz functions for ^{31}P and ^{29}Si MAS NMR spectra and the Q MAS ½ model and Gauss/Lorentz functions for the ^{11}B resonances of three- and four- coordinated boron species, respectively. N_4 values were determined from the ratio of the integrated areas of the peaks attributed to the four-coordinated

boron species as compared to the total integrated area of central transition peaks, including a small correction for the overlapping satellite transition of the B(IV) species.[55]

Table 2. Summary of measurement conditions for all the nuclei studied by MAS NMR.

Single Resonance Parameters		
^{23}Na	Magnetic field (T) / Resonance frequency (MHz)	5.7 / 64.1
	Spinning frequency (kHz)	25.0
	Pulse length (μs) / Tip angle	0.8 / (π/6)
	Recycle delay (s)	0.5
	Number of acquisitions	≥4000
	Reference standard	NaCl (7.2 ppm)
^{11}B	Magnetic field (T) / Resonance frequency (MHz)	14.1 / 192.6
	Spinning frequency (kHz)	15.0
	Pulse length (μs) / (Tip Angle)	1.0 / (π/6)
	Recycle delay (s)	15
	Number of acquisitions	≥100
	Reference standard	BPO_4 (-3.5 ppm)
^{31}P	Magnetic field (T) / Resonance frequency (MHz)	5.7 / 98.1
	Spinning frequency (kHz)	10.0
	Pulse length (μs) / (Tip angle)	2.9 / (π/2)
	Recycle delay (s)	150
	Number of acquisitions	≥400
	Reference standard	BPO_4 (-29.3 ppm)
^{29}Si	Magnetic Field (T) / Resonance frequency (MHz)	9.4 / 79.5
	Spinning frequency (kHz)	4.5-4.7
	Pulse length (μs) / (Tip angle)	5.5 / (π/2)
	Recycle delay (s)	150
	Number of acquisitions	≥20
	Reference standard	Kaolinite (-91.5 ppm)

Additionally, ^{1}H→^{31}P and ^{1}H→^{29}Si cross-polarization (CP) MAS NMR and ^{11}B{^{1}H} rotational echo double resonance (REDOR) experiments were performed to assess the structural changes occurring in the hydrated surface layers exposed to simulated body environments. The ^{1}H→^{31}P CP-MAS NMR experiments were performed for selected samples on a 5.7 T Varian 240-MR DD2 spectrometer (242.4 MHz and 98.1 MHz resonance frequencies for ^{1}H and ^{31}P, respectively) using a commercial 3.2 mm triple resonance MAS NMR probe. The powdered samples were packed into zirconia rotors and spun at a MAS frequency of 10.0 kHz. The matching

conditions for CP experiments were optimized with regard to solid NaH_2PO_4. Contact times between 300 and 1500 μs were used along with π/2 radio frequency pulses of 4.3 μs duration. Recycle delays of 1 s were used, with a minimum of 27000 acquisitions collected per sample. The measured ^{31}P chemical shifts are reported relative to 85% H_3PO_4 using solid BPO_4 as a secondary standard at -29.3 ppm.

The $^{1}H \rightarrow ^{29}Si$ CP-MAS NMR experiments were performed for selected samples on a 9.4 T Varian Unity INOVA spectrometer (400.1 MHz and 79.5 MHz resonance frequencies for ^{1}H and ^{29}Si, respectively) using a 7 mm CP-MAS probe. The powdered samples were packed into silicon nitride rotors and spun at 4.5 to 4.7 kHz. The matching conditions for CP experiments were optimized on solid kaolinite. Contact times of 3000 μs were used following ^{1}H π/2 preparation pulses of 6.8 μs duration. A minimum of 1600 scans were acquired, using a relaxation delay of 5 s. The measured ^{29}Si chemical shifts are reported relative to tetramethylsilane, using solid kaolinite as a secondary standard at -91.5 ppm.

$^{11}B\{^{1}H\}$ REDOR experiments were performed at 14.1 T and ν_{MAS} = 15 kHz on a Bruker Neo 600 Spectrometer, using a commercially available 1.3 mm triple-resonance MAS Probe. The standard sequence of Gullion and Schaefer was used,[56] employing ^{11}B and ^{1}H π-pulses of 1.8 and 3.7 μs, respectively (selective excitation limit for the ½ ↔ -½ transition of the B(III) species). Prior to the measurements, the samples were heated at 250 °C for 24 h to remove surface-adsorbed water and traces of residual Tris buffer from the dissolution process.

4.3.3 Compositional and microstructural evolution of the monolithic glass coupons during degradation processes

The degradation experiments were additionally performed on polished monolithic coupons of glasses MB2-P5 and PB2-P5 (two per composition) for 3- and 7-day durations. The recovered

coupons were subjected to the same drying procedure as was performed for the recovered glass powders.

X-ray photoelectron spectroscopy (XPS) measurements were performed on monolithic glass coupons to understand the elemental composition and speciation within the top 10 nm of sample surfaces – both in polished and degraded samples. The XPS measurements utilized a Thermo Scientific K-Alpha instrument, which used a 1486.6 eV monochromatized Al K_α X-ray source to excite core level electrons from the sample. The details of the equipment and experimental protocols were similar to those reported in our previous studies.[50, 57] The probe depth of XPS, taken to be three times the inelastic mean free path of photoelectrons, was 3.6 nm for Na 1s, 8.7 nm for P 2p, 6.9 nm for O 1s, and 9.3 nm for B 1s and Si 2p electrons.

Further, the water uptake in the surface layers of the dissolved glass coupons was analyzed by collecting the hydrogen profiles on the surface of post-degradation samples by elastic recoil detection analysis (ERDA) using a 2.0 MeV He^{++} beam (General Ionex Tandetron accelerator), as has been discussed in our previous studies.[50, 57] The probe depth of ERDA is approximately 350 nm.

The PB2-P5 glass coupon recovered from 7 days of degradation experiments was mounted vertically in epoxy resin and polished to a mirror finish (in non-aqueous media) to examine its cross-section and determine the depth and characteristics of the hydrated surface layers. The sample surface was sputter-coated with a 20 nm thick gold layer to reduce the charging effects. Both secondary electron imaging (ZEISS Sigma) and energy dispersive spectroscopy (EDS; X-Max Oxford Instruments; Aztec software) were performed using an electron beam of 10-20 kV. EDS was employed to perform elemental mapping in the hydrated layers of the glass to assess

compositional differences between the pristine and dissolved glass and supplement our understanding of the dissolution mechanisms and surface layer formation.

5. Results

5.1 Glass formation

The glasses selected for degradation experiments were visibly transparent and did not show any evidence of crystallinity in the XRD data, as shown in Figures S1 and S2, respectively. It was observed that series MB2-P*x* and PB2-P*x* can incorporate up to 5 mol. % P_2O_5 while peralkaline series of glasses (PA2-P*x*) can only incorporate up to 3 mol. % P_2O_5 before visible phase separation and/or crystallization. The absence of visible glass-in-glass phase separation and lack of XRD patterns characteristic of $Na_4P_2O_7$ phases (as observed in previously-reported translucent samples[35]) allows for an unambiguous examination of degradation behavior and structural evolution of the present samples. The experimentally measured glass compositions are displayed in Table 1 and show close agreement (within ±0.6 mol.%) of their batched targets for B_2O_3 and P_2O_5. Experimental Na_2O and SiO_2 contents similarly display close agreement with the batched compositions (within ±0.5 mol.%) in the baseline glasses, however, larger differences in their content are evident in P_2O_5-containing samples (ranging between ±0.7 and 2.7 mol.% in glasses with x = 3-5 mol.%).

5.2 Glass structure vs. T_g

The evolution in short-to-intermediate-range ordering in the structure of these glasses as a function of P_2O_5 content has been extensively studied and reported in our previous article.[35] The network forming units (NFUs) have been labeled in terms of T^n (T = Si, B, P), where n denotes the numbers of bridging oxygen atoms to other T species. It has been shown that in glasses with lower

P_2O_5 content (x = 1), phosphate units are dominantly present as isolated species (P^0 and P^1). Glasses with x > 1, on the other hand, exhibit increased P–O–B linkages with P^2 or P^3 species, linked to P, Si, and B(IV), promoting a re-distribution of Na^+. This is accompanied by an increased degree of polymerization of silicate units and a decrease in the N_4 (fraction of tetrahedral boron) units. $<n_P>$, the average number of bridging oxygen around each phosphorus, are listed in Table 1. Furthermore, it was observed that the fraction of four-coordinated boron species, N_4, increases in the order PB < MB < PA, (as also displayed in Table 1), which is largely driven by the Na_2O/B_2O_3 ratio (R). Finally, for all the glasses, the average number of bridging oxygen per silicon atom, $<n_{Si}>$, increase with increasing P_2O_5 content, reflecting the well-known tendency of phosphorus oxide to act as an alkali metal scavenger in multiple network former glasses, *i.e.*, to attract the network modifier species preferentially.

The data pertaining to the short-to-intermediate ordering in the glass structure can be correlated with the trends observed in their T_g values, as presented in Figure 1a. The successive addition of P_2O_5 in perboric (PB2-Px) glasses results in an almost linear decrease in T_g from 558 ºC to 505 ºC. In the case of metaboric glasses, the initial addition of P_2O_5 (1 mol.%) to the base glass results in a decrease in T_g from 560 °C to 542 °C. However, the T_g remains relatively constant upon further increases in P_2O_5 content in the glasses. Finally, for peralkaline glasses, P_2O_5 additions seem to have an insignificant impact on their T_g values.

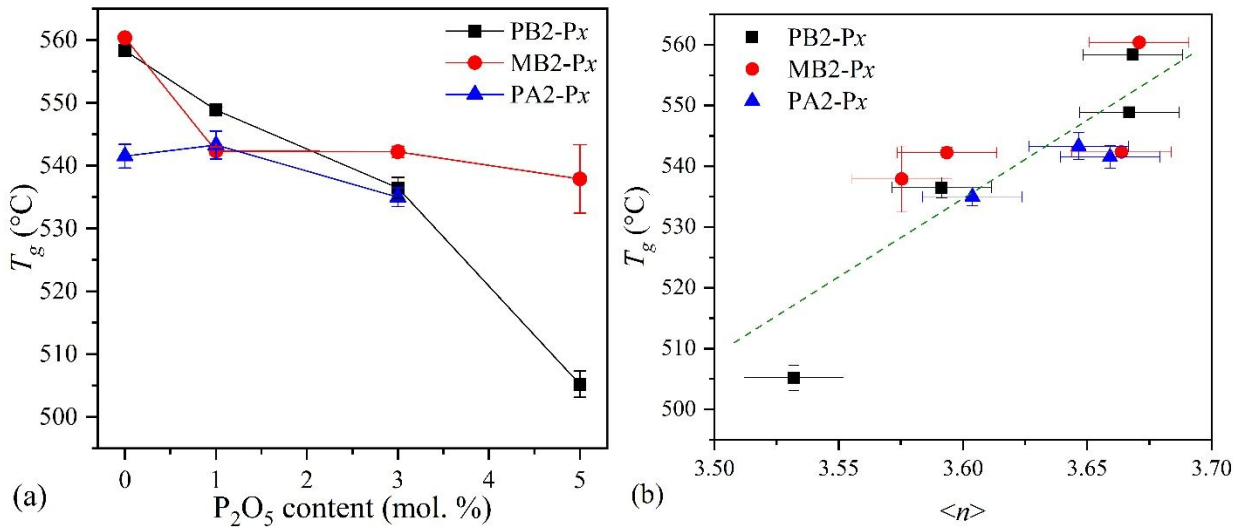

Figure 1. (a) T_g vs. P_2O_5 content for PB2-P*x*, MB2-P*x*, and PA2-P*x* glasses and (b) T_g vs. <*n*>, the average network former coordination number, as calculated using equation (2). The dashed line depicts a linear regression fit to the data.

When trying to understand the trends in T_g with respect to the structural evolution in glasses, it is well-known that T_g values can be correlated with features like bond strength, network connectivity, and network structural rigidity.[58-60] For instance, fully polymerized B(IV) and Si^4 species in the glass network tend to increase the T_g,[61, 62] whereas network forming units (NFUs) containing non-bridging oxygen (NBO), *i.e.*, low connectivity phosphate species (P^0 and P^1), tend to decrease it.[63] For this reason, the low average phosphate connectivity (1.23-1.74) in P_2O_5-containing glasses, as observed in Table 1, although rising with P_2O_5 content due to the formation of significant fractions of P–O–B(IV) linkages, is expected to have an overall negative impact on T_g across each series. Nevertheless, the introduction of P_2O_5 also has different effects on the borate and silicate networks, which is evident from the contrasting T_g behaviors between the glass series with different *R* regimes (Figure 1a). Therefore, the observed T_g trends can be rationalized based upon the relative fraction of silicate and borate species in the glass structure and the distribution of Na^+ in the glass network. For example, perboric glasses have higher overall borate contents, thus T_g is more impacted by the decrease in average boron coordination number and borate

connectivity in these glasses compared to their peralkaline counterparts. Furthermore, the significant increase in the fraction of P–O–B(IV) linkages observed in perboric glasses (see Table 1) likely induces further Na^+ re-distribution towards P–NBO or Si–NBO sites. Based on bond valence considerations, P–O–B(IV) linkages do not require charge compensation for the tetrahedral boron site, as the bridging oxygen linking these two species is essentially charge-balanced owing to the bond valence gradient present. On the other hand, changes in the borate network of metaboric and peralkaline glasses have less of an effect upon T_g values. In these regimes, the increasing fractions of silicate network species more effectively counterbalance changes in the borate network.

Putting each of these considerations into quantitative terms, Figure 1b shows a good correlation of T_g with the average network former coordination number $<n>$, which is calculated from Table 1 using equation (2):

$$<n> = (2[B_2O_3]<n_B> + 2[P_2O_5]<n_P> +[SiO_2]<n_{Si}>)/(2[B_2O_3] + 2[P_2O_5] + [SiO_2]) \qquad (2)$$

From this correlation, it is evident that phosphorus incorporation into these borosilicate glasses tends to decrease the average coordination number, producing a systematic decrease of T_g in all three series.

5.3 Elemental release behavior of glasses in Tris buffer solutions

Table S1 summarizes all the temporal evolutions of pH, elemental concentrations, and normalized losses (NL) for each glass composition. Throughout 28 days of exposure, the solution pH rises only slightly towards a constant value between 7.3 and 7.7, indicating that the Tris-HCl and Tris-HNO_3 solutions exhibit a good buffering ability and can closely replicate the pH of human body fluids. Figures 2(a-f) display NL vs. time curves of glasses with minimum (x = 0) and maximum (x = 3 or 5 mol.%) concentrations of P_2O_5 submerged in Tris-HNO_3 solutions. All

glasses display a clear linear, forward release behavior within the first 12 to 24 hours, followed by a rate drop and rapid or gradual transition into the residual rate regime, typically attributed to the presence of a passivating gel layer on the surface of the glass and/or solution saturation with silica species.[64, 65] The residual rate regime is reached within 3-14 days of immersion, depending on the glass composition and dissolution kinetics. As expected, the sodium borosilicate compositions ($x = 0$) exhibit very similar NL of Na and B, marked by rapid elemental release kinetics, while Si is released from the glasses at a much lower rate. This is evidenced by the 3-4 mol/m^2 NL values of Na and B after 28 days in glasses with $x = 0$ as compared to 0.8-1.1 mol/m^2 for Si (see Figure 2a, c, and e). The magnitude of release is also observed to be highly dependent on the R compositional regime, which will be discussed in the following sections. Upon the addition of P_2O_5 in the glass, P release closely follows that of Na and B in all the compositions. Thus, a close overlap of Na, P, and B release data signifies their congruent dissolution from the glass.

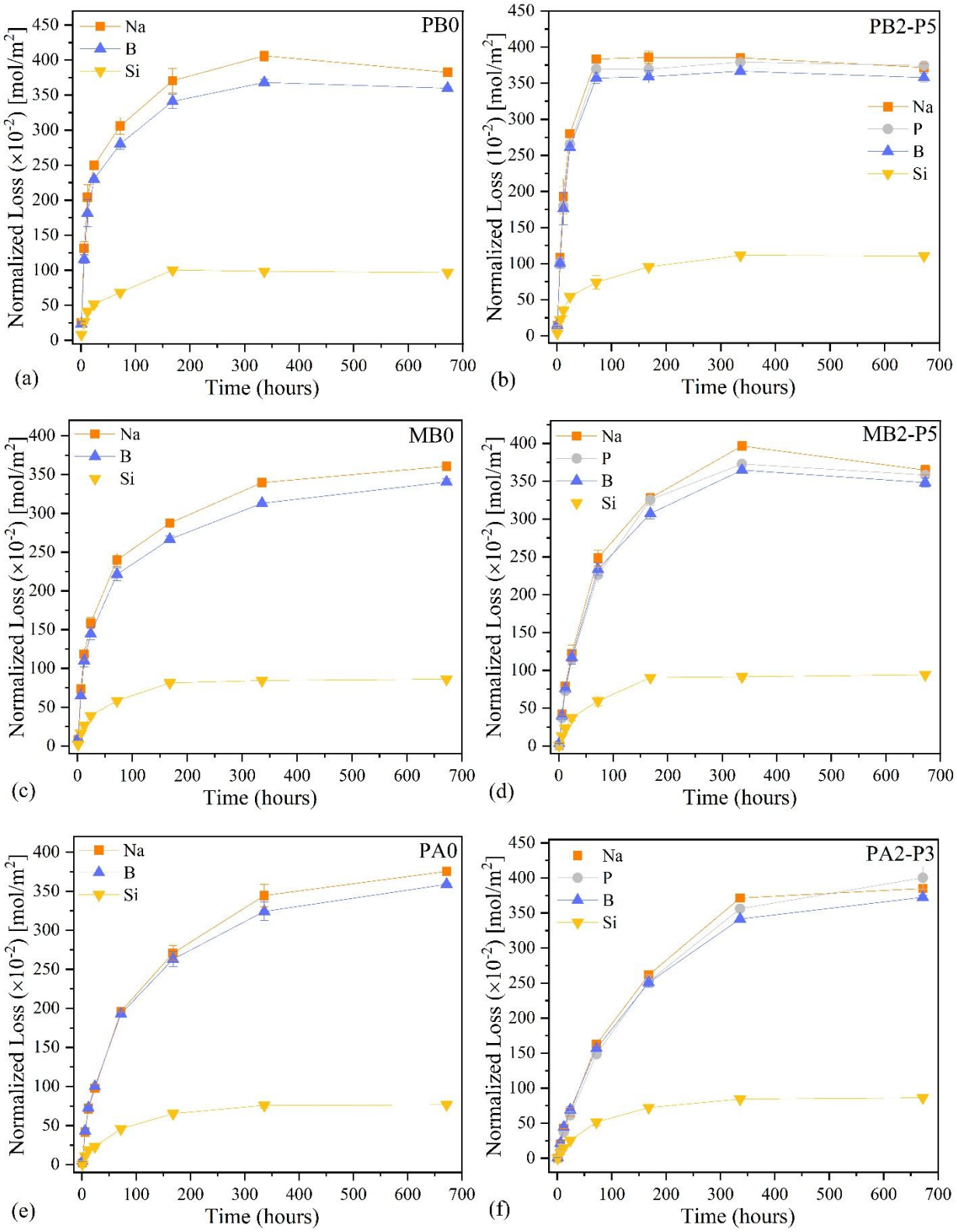

Figure 2. Plots of normalized loss (in units of 10^{-2} mol/m^2) vs. time (hours) for each element present in the glass for (a) PB0, (b) PB2-P5, (c) MB0, (d) MB2-P5, (e) PA0, and (f) PA2-P3.

To quantify the glass dissolution kinetics and estimate the forward rate, the initial portions of the NL data have been fit using linear regression (within the first 12 hours of experiments) and the extracted rates are displayed in Table 3. These values represent the maximum expected degradation rates of the studied glasses. The error expressed in the table represents standard uncertainty in linear regression, where the standard deviation of each NL data point has been considered, and the relative impact of fitting a slope to uncertain data has been summed to determine the overall fitted-slope uncertainty, similar to the method discussed by Kragten.[66] In general, it is observed that the dissolution rate of the glasses is highly dependent on their compositional regime and ranks in the order PA < MB < PB. Figure 3a graphically depicts the Na and B dissolution rates of the glasses (in Tris-HNO_3) in each compositional regime as a function of P_2O_5 content. The release rates of Na, P, and B show good agreement and range between 0.04-0.06 $mol \cdot m^{-2}h^{-1}$ for PA glasses, 0.04-0.11 $mol \cdot m^{-2}h^{-1}$ for MB glasses, and 0.15-0.17 $mol \cdot m^{-2}h^{-1}$ for PB glasses. The silicate species are consistently released from the glasses at rates varying between 0.01-0.03 $mol \cdot m^{-2}h^{-1}$.

Table 3. Degradation rates of Na, P, B, and Si for the studied glasses in simulated body environments. These rates were determined by applying a linear approximation to the initial regime (first 12 hours) of the normalized loss vs. time plots.

		Degradation Rates ($\times 10^{-2}$; mol□glass/[m^2h])							
Sample ID	**Solution**	**Na**	**Na-error**	**P**	**P-error**	**B**	**B-error**	**Si**	**Si-error**
PB0	Tris-HNO_3	16	±2	--	--	14	±2	3.0	±0.3
PB2-P1		17	±2	16	±2	15	±1	2.9	±0.4
PB2-P3		16.5	±0.5	15.2	±0.9	14.7	±0.5	3.1	±0.1
PB2-P5		16	±2	15	±2	16	±2	2.8	±0.7
MB0	Tris-HCl	8.5	±0.2	--	--	7.2	±0.2	2.08	±0.01
MB2-P1		8.3	±0.3	6.9	±0.2	6.8	±0.2	1.6	±0.1
MB2-P3		7.2	±0.4	6.6	±0.4	6.0	±0.4	1.87	±0.02
MB2-P5		4.4	±1.1	4	±1	3.7	±0.9	1.1	±0.5
MB0	Tris-HNO_3	9.9	±0.7	--	--	9.1	±0.7	2.2	±0.3
MB2-P1		11.0	±0.2	9.4	±0.6	9.6	±0.2	2.1	±0.1
MB2-P3		10.0	±0.2	9.0	±0.1	9.0	±0.2	2.4	±0.1
MB2-P5		7.09	±0.03	6.5	±0.1	6.59	±0.04	2.1	±0.1
PA0	Tris-HNO_3	6.3	±0.6	--	--	6.2	±0.3	1.6	±0.3
PA2-P1		5.8	±0.2	4.44	±0.03	5.7	±0.2	1.84	±0.06
PA2-P3		3.84	±0.04	3.42	±0.04	3.94	±0.09	1.33	±0.05

The impact of P_2O_5 addition on the degradation behavior shows a considerable dependence on their Na_2O/B_2O_3 ratio. P_2O_5 does not exhibit a significant impact on the dissolution kinetics of glasses in the perboric (Na/B < 1) regime (Figure 3a). On the other hand, the degradation rates of metaboric (Na/B = 1) and peralkaline (Na/B > 1) glasses decrease with increasing P_2O_5 content, with a steeper and more linear decrease in the latter. Again, following previous suggestions in the literature,[67-69] the connectivity information listed in Table 1 provides a useful rationale for explaining these trends. As the experimental results clearly show that the B_2O_3 content in the glasses significantly impacts their initial dissolution rates and since the local structure around boron is also greatly impacted by phosphate network incorporation, it is vital to explore the correlation between dissolution kinetics and borate presence/connectivity. Accordingly, Figures 3b-I and 3b-II illustrate excellent linear correlations between the dissolution rate of Na from the glass (which dissolves concurrently with both B and P) and $\langle f_B \rangle$, the fraction of B of all NFUs, and $(\langle f_B \rangle \langle n_B \rangle) / \langle n_{B,Mean} \rangle$, respectively. In the latter term, $\langle n_B \rangle$ indicates the average connectivity

of boron in the individual glass and $<n_{B,Mean}>$ is a constant (the average $<n_B>$ for all compositions is equal to 3.664) which serves as a scaling factor and allows for a direct comparison between the slopes of Figure 3b-I and 3b-II. Accordingly, linear regression performed on each plot displays a highly linear trend ($R^2 > 0.91$), where Figure 3b-I indicates the strong correlation between the amount of boron in the network and the dissolution rate, driven by fast hydrolysis of borate units. However, by incorporating the term $<n_B>$ into Figure 3b-II and appropriately scaling the *x*-axis, we deduce from the noticeably larger slope in this figure (83.2 vs. 77.7) that $<n_B>$, along with $<f_B>$, additionally impacts the dissolution rate of the glass. These results signify that although the relative fraction of boron NFU species acts as the main driving factor controlling dissolution rates, changes in the local structure around boron species similarly correlate with rate increases. Finally, we note that the very similar dissolution rates as measured for boron and phosphorus are not unexpected given the strong B–O–P connectivity encountered in these glasses. Thus, the majority of phosphate units from the glasses can only be released concurrently with the boron species they are bonded to.

Figure 3c displays a comparison between the dissolution rates of Na, B, and Si extracted from MB glasses (as a function of P_2O_5 content) in Tris-HCl and Tris-HNO_3 solutions, where all other experimental parameters (*i.e.*, temperature, pH, SA/V, etc.) have been carefully controlled and held constant. Interestingly, it is observed that the degradation rates of borosilicate glasses are higher in Tris-HNO_3 solutions as compared to Tris-HCl solutions, which is contrary to the results reported by Tournié et al.[53] While these kinetic changes are statistically significant based upon the current error analysis, it is uncertain if Tris-HCl vs. Tris-HNO_3 rates are appreciably different, given the 15-25 % systematic errors typically associated with the dissolution experiments[70-72] and the approximation involved in fitting NL data with a single rate.[73, 74] Accordingly, many—but not

all—of the rate differences reported in Tris-HCl vs. Tris-HNO_3 for the current compositions are within the usually attributed errors in dissolution experiments. Furthermore, a close agreement is observed for the NL values within the residual rate regime. Thus, further work is needed to clarify the influence of acid identity on the dissolution process.

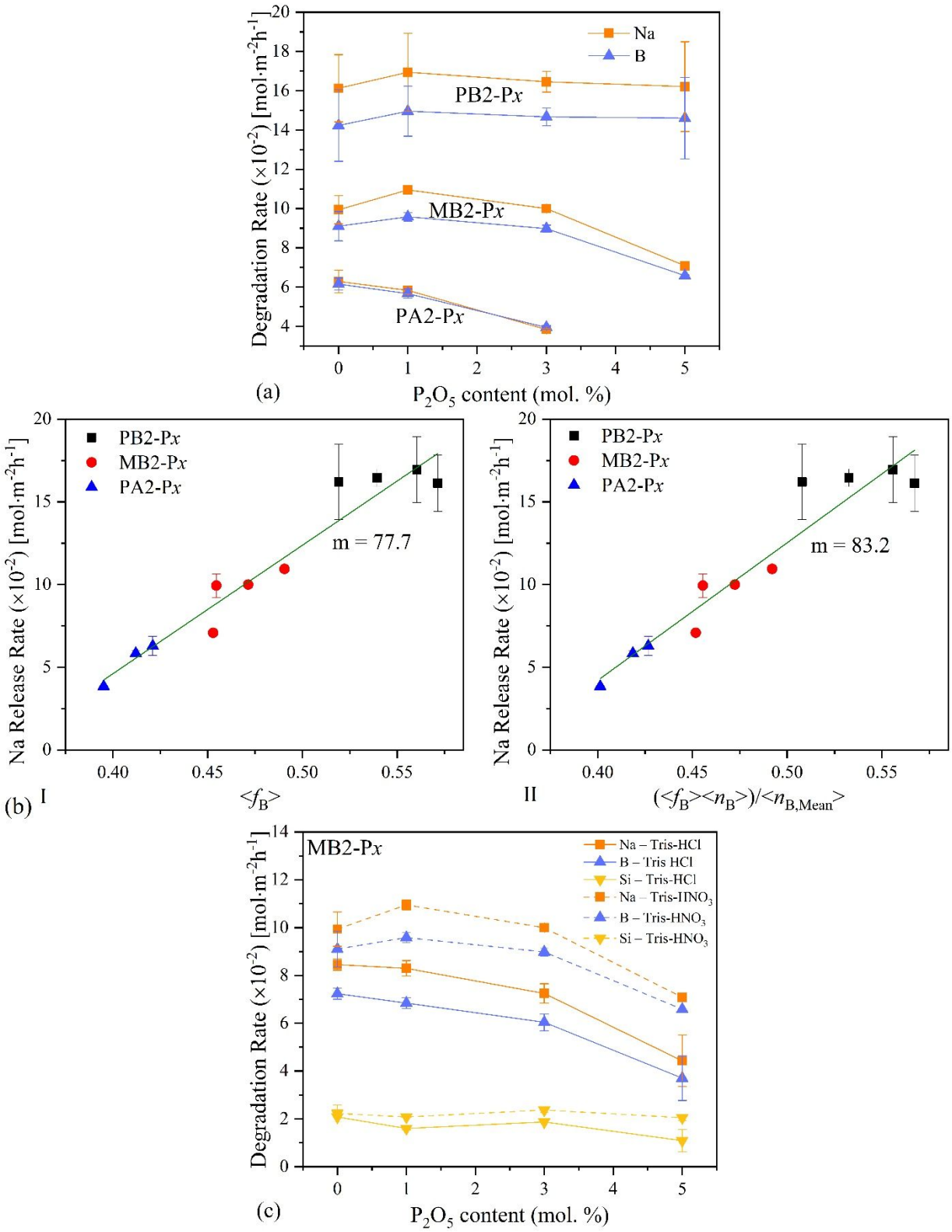

Figure 3. Degradation rates (in units of 10^{-2} mol·m^{-2}h^{-1}) (a) as a function of P_2O_5 content for Na and B for all glasses in Tris-HNO_3, (b)-I as a function of $\langle f_B \rangle$ the fraction of B NFU species, and (b)-II as a function of $(\langle f_B \rangle \langle n_B \rangle) / \langle n_{B,Mean} \rangle$, the product of $\langle f_B \rangle$ and $\langle n_B \rangle$, the average boron

connectivity for each glass, scaled by $<n_{B,Mean}>$, the average boron connectivity for all studied compositions, for Na for all glasses in Tris-HNO_3, and (c) for Na, B, and Si for MB2-P*x* glasses in Tris-HCl and Tris-HNO_3 environments.

5.4 Structural evolution of the glass and surface layers during dissolution processes

The glass powders recovered from degradation experiments were first analyzed by XRD for the presence of any crystalline secondary phases. As shown in Figure S3, all the samples remain amorphous after degradation in the buffer solutions. Thus, to understand the evolving amorphous structure (in the top ~10-15 μm of the surface and in the bulk) of the glasses as a function of chemical degradation, FTIR and MAS NMR spectroscopic experiments were performed on the pre- and post-degradation glass particles. Figure 4 displays a comparison between the baseline-subtracted FTIR spectra of the as-synthesized PB2-P5 glass and those obtained on the glass particles recovered from buffer solutions at time intervals varying between 1 hour and 28 days. Due to the ATR measurement mode, these spectra selectively monitor the development of the surface layer. As the duration of dissolution progresses, the FTIR spectra undergo significant changes in the region of 850-1200 cm^{-1}, marked by two evident bands (955 and 1055 cm^{-1}) and a shoulder at 1220 cm^{-1} which begin to emerge after 1 day and grow with further exposure time. These bands at 955, 1055, and 1220 cm^{-1} are associated with stretching vibrations of NBO or Si–OH groups,[75, 76] asymmetric stretching and vibrations of bridging oxygen,[76] and asymmetric Si–O–Si stretching,[75, 77] respectively. The observed structural changes are consistent with the beginning of the transitional "rate drop" regime (as displayed in Figure 2b) where the glass begins to progress from the forward rate regime to the slower residual rate regime, caused by the formation of a silica gel layer on the glass surface which evolves with increased thickness, as a function of dissolution time.[40, 75, 77] This attribution is further supported by the development of a minor peak near 1630 cm^{-1} and a broad peak in the higher frequency region centered near 3350

cm^{-1}, attributed to the presence of H_2O bending modes and H_2O and OH stretching modes, respectively.[75-78] Further, the emerging and growing peaks at 450, 560, and 795 cm^{-1} are likely attributed to greater fractions of silica species in the surface layers, as various bending and stretching modes of Si-bonded bridging and NBO species have been observed in these regions for silica gel layers.[75] Alongside the emergence of silica-related bands, increased dissolution time leads to a decrease in the intensity of bands associated with borate units, namely a weak shoulder centered at 690 cm^{-1} associated with metaborate species and a broad band centered at 1380 cm^{-1} which may be associated with several borate structural units.[79, 80] The aforementioned borate bands are not evident in samples recovered from the dissolution experiments lasting longer than 1 day.

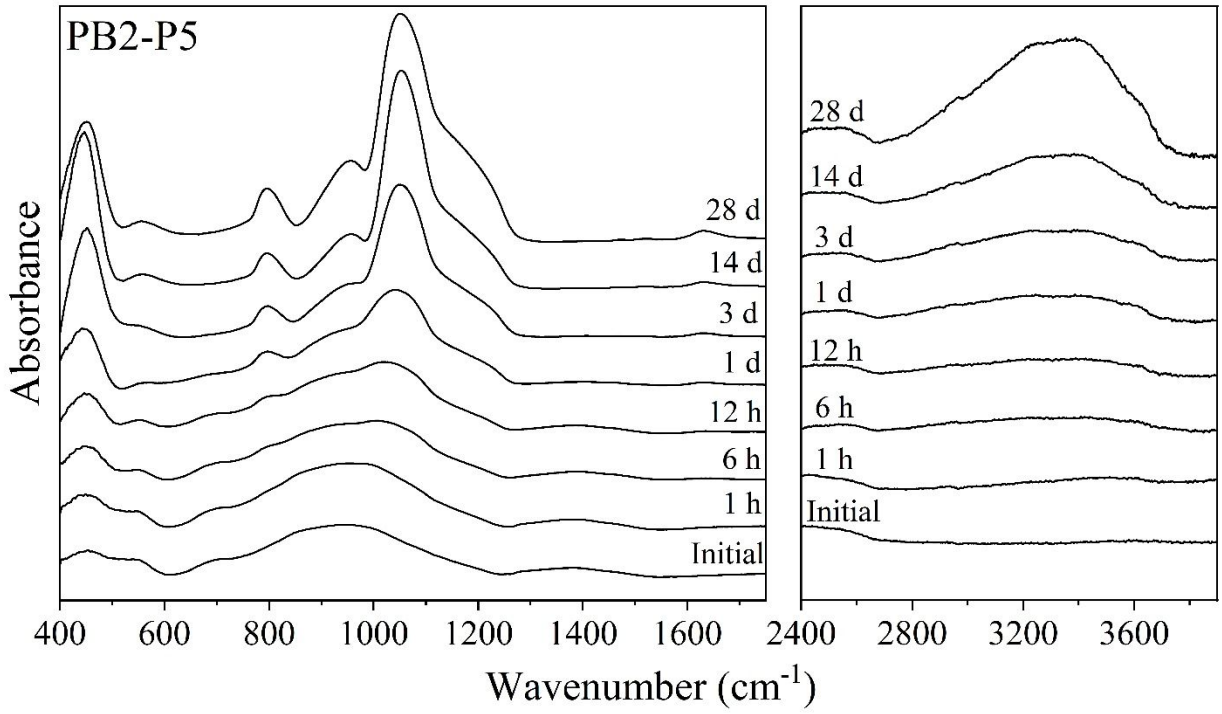

Figure 4. FTIR spectra of PB2-P5 glass before and after immersion in Tris-HNO_3 for 1 h to 28 days.

To further evaluate the structural evolution in glasses as a function of dissolution time, multinuclear MAS NMR spectroscopic techniques were utilized. Figure 5 displays the ^{11}B MAS NMR spectra and fittings of PB samples dissolved in Tris-HNO_3 for 7 days (as compared to the

spectra of the initial glass). Similar spectral comparisons for MB and PA samples (as-synthesized vs. samples recovered after 7-day experiments) are depicted in Figures S4 and S5, respectively. These spectra display two main resonances: a broad feature centered near 14 ppm and a narrower peak in the region 0-3 ppm consisting of multiple underlying species. The feature near 14 ppm is associated with B(III) species, which consists of overlapping ring- and non-ring trigonal boron species. Nevertheless, this broad lineshape component may also contain unresolved B(III) species bound to an NBO. Therefore, the ~14 ppm peak has accordingly been fitted using two distinct second-order quadrupolar lineshape components (using Q mas ½ functions in DMfit), encompassing ring- and non-ring B(III) species. The N_4 values for the glass particles recovered after 1 and 7 days in Tris-HNO_3 environments (as compared to the initial glass) are presented in Table 4, and the fitting parameters are listed in Table S2. In general, N_4 values rise as a result of the dissolution process, by as much as 4% in 1-day samples and 33% in 7-day samples, as compared to the initial glasses. N_4 values change most significantly in glasses undergoing rapid network dissolution, *i.e.*, the corresponding rates follow the order PA < MB < PB. Accordingly, comparing the spectra of the parent glass with that obtained after 7 days of dissolution (see Figure 5 and Figures S4 and S5), it is observed that the intensity of the B(III) peak decreases in all cases, with the most significant spectral changes occurring for PB samples. For instance, the B(III) signatures in the PB2-P3 and PB2-P5 glasses exposed to Tris-HNO_3 for 7 days are very minor. Furthermore, the displayed spectra do not undergo any apparent shape change in the B(III) signals following glass dissolution, as highlighted by their simultaneous reductions in peak area (see Table S2). On the other hand, the peaks associated with the B(IV) units show clear changes in shape, particularly evidenced in the PB glasses (Figure 5). A careful analysis of this region using DMFit was guided by the fittings performed for the as-synthesized samples (as published in Ref.[35]), where

the full-width half-maxima (FHWM) and position of the two previously identified components (hereafter labeled B(IV)-a and B(IV)-b, respectively) were held roughly constant, allowing their intensity to vary. This analysis indicated the development of an additional sharp peak (FWHM = 0.8-1.0 ppm) centered at -1.1 to -1.2 ppm (hereafter labeled B(IV)-c) in the PB and MB glass samples recovered after 7 days of dissolution, suggesting the presence of a new distinct four-coordinated boron species. The fitted B(IV) components mentioned here are labeled as 'a', 'b', and 'c' in Figures 5 and S4. Further, it is evident from the deconvolutions displayed in Figure 5 that the intensity of the B(IV)-c peak grows with increases in P_2O_5 content in the glass (see Table S2). Additionally, it is observed that the broader B(IV)-a and B(IV)-b peaks reduce significantly in intensity for the 7-day samples PB2-P3 and PB2-P5 (Figure 5c and d), as compared to the lower P_2O_5 content PB0 and PB2-P1 (Figures 5a and b) glasses. The ^{11}B MAS NMR spectra of glasses MB2-P1, MB2-P3, and MB2-P5 degraded in Tris-HNO_3 for 7 days similarly depict a B(IV)-c peak, however, the spectral changes are not as evident or significant (Figure S4). The ^{11}B MAS NMR spectra of glass particles from series PA2-P*x* recovered after 7 days of dissolution did not display any evidence of a similar peak (see Figure S5).

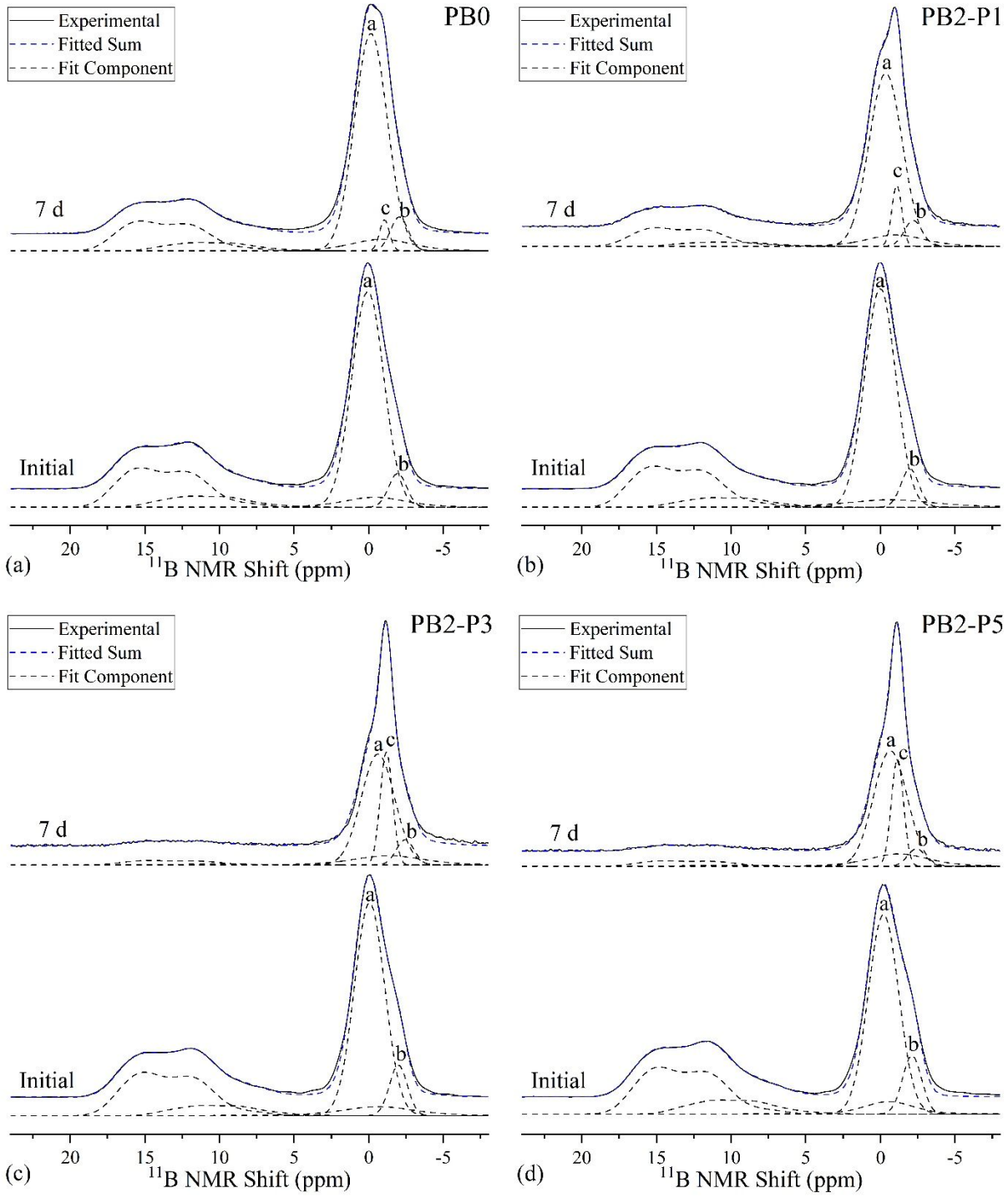

Figure 5. ^{11}B MAS NMR spectra and subsequent lineshape fitting of the as-synthesized (a) PB0, (b) PB2-P1, (c) PB2-P3, and (d) PB2-P5 glasses as compared to analogous glass powders recovered from 7 d degradation experiments in Tris-HNO_3 solutions.

Table 4. N_4 values (in percent) of the initial glasses and the powders recovered from 1- and 7-day degradation experiments in Tris-HNO_3 environments.

Sample ID	^{11}B MAS NMR		
	Initial	1 day	7 days
PB0	63.7	65.2	72.0
PB2-P1	63.4	67.3	78.3
PB2-P3	61.8	64.5	92.7
PB2-P5	58.5	60.5	91.3
MB0	67.2	69.5	72.8
MB2-P1	67.5	68.6	73.7
MB2-P3	67.2	68.7	74.9
MB2-P5	65.5	64.7	70.6
PA0	71.3	72.4	74.2
PA2-P1	72.2	72.8	75.8
PA2-P3	72.2	72.7	75.5

The results from ^{11}B MAS NMR (as discussed above) indicate that the glasses undergo preferential dissolution of B(III) species as compared to B(IV). In addition, with regard to the emergence of the newly observed B(IV)-c species, there are two possible scenarios: (i) they represent species present in the original glass which dissolve more slowly compared to the other B(III) and B(IV) units, thus, becoming more clearly visible in the spectra of the exposed samples, or (ii) they represent a new surface species (or even a precipitated boron-containing secondary phase) generated due to the interaction of the glass with the buffer solution. Although precipitated borate species have been hypothesized/demonstrated in the literature discussing glass dissolution behavior in highly alkaline solutions (pH > 10.5),[50, 81-83] their formation is not expected in near-neutral environments, and thus will not be considered here. It is known from the literature on sodium borosilicate glasses that both B(III) and B(IV) species can have distinctly different chemical shifts depending on the identity of the next-nearest neighbor species. For instance, in our system, it is expected that the resonances associated with multiple combinations of B(IV)–O–B(III), B(IV)–O–Si, and B(IV)–O–P linkages all occur within the region -2 to +1 ppm, as has been

shown by Du and Stebbins[84] who attributed a peak near -2 ppm to $B(IV)_{0B,4Si}$, whereas a greater fraction of B–O–B linkages would lead to more positive chemical shifts. Furthermore, it can be inferred from the previous study of the structure of these glasses that a peak observed near -1 ppm is likely not associated with B(IV)–O–P linkages.[35] Additionally, the ^{31}P MAS NMR experiments on the recovered PB2-P5 7 d sample indicate the absence of phosphate species remaining in the dissolved glass (see Figure S6). Rather, this species is presumably associated with $B(IV)_{4Si}$ species pinned within the hydrated silica network. In an attempt to confirm this peak assignment, ^{11}B-^{29}Si REDOR experiments were performed on sample PB2-P5 (before and after 7 days of dissolution; data not shown). However, the results from the ^{11}B-^{29}Si REDOR experiments remain inconclusive due to the low natural abundance of ^{29}Si and require further investigation using ^{29}Si-enriched glasses. Further, in an effort to attribute the emergent B(IV)-c component to a newly created surface species, the strength of the ^{11}B-^{1}H magnetic dipole-dipole coupling due to hydrous species was examined for the sample PB2-P3 using $^{11}B\{^{1}H\}$ REDOR NMR spectroscopy. Figure 6a shows the full REDOR curves (normalized difference signal $(S_0-S)/S_0$ versus dipolar mixing time) for the initial (unexposed) sample, the sample exposed for 7 d, and the model compound $B(OH)_3$. While the unexposed sample shows no ^{11}B-^{1}H interactions, as expected, there is clear evidence for such interactions in the REDOR curves of the sample exposed to Tris-HNO_3 solution for 7 days. This concerns both the B(III) and the B(IV) species. Figure 6a also shows the REDOR curve for the model compound $B(OH)_3$ which displays the strong dipolar dephasing expected due to the presence of three B–OH linkages. Further insights are possible by considering the Fourier Transforms of the S_0, S, and ΔS signals, shown in Figure 6b as obtained from the REDOR curves for dipolar mixing times around 1.07 ms. To improve the signal-to-noise ratio, seven S_0 and S spectra were co-added (5th – 11th REDOR data points). It is worth noting that the fraction of B(III)

species appears considerably larger in the S_0 spectra as compared to the single-pulse spectra. This enhancement is due to the chosen ^{11}B spin echo pulse durations which, while resulting in 90° and 180° flip angles for the B(III) central transition, correspond to smaller flip angles for the B(IV) units, for which the effective nutation frequency is lower because the satellite transitions are partially excited. This situation results in an effective reduction of the B(IV) spin echo intensity relative to the B(III) spin echo intensity; in addition, differences in spin-spin relaxation times may contribute to this effect.

For further analysis, the co-added spectra were then simulated by assuming four lineshape components (two for B(III) and two for B(IV) with identical parameters between S_0 and S, while optimizing the areas of the respective components. Finally, the difference spectrum ΔS was created by subtracting the co-added S spectra from the co-added S_0 spectra and fitted by the same deconvolution model. Within the limited resolution and signal-to-noise ratio available, it is not possible to reveal clearly different REDOR behaviors for the three distinct B(IV) units a-c identified in the single-pulse spectra. On the other hand, the REDOR experiments allow a clear distinction between two types of B(III) units differing in their dipolar coupling strength with ^{1}H nuclei from the hydrous species: the component at an isotropic chemical shift of 18.2 ppm is emphasized in the ^{11}B{^{1}H} REDOR difference spectrum, suggesting that this species has a significantly stronger interaction with ^{1}H than the B(III) units giving rise to the low-frequency component near 13.3 ppm, which is emphasized in the spectrum with dipolar dephasing. We attribute the 18.2 ppm peak to B(III) units within the hydrated layers where they may be bonded to hydroxyl groups.

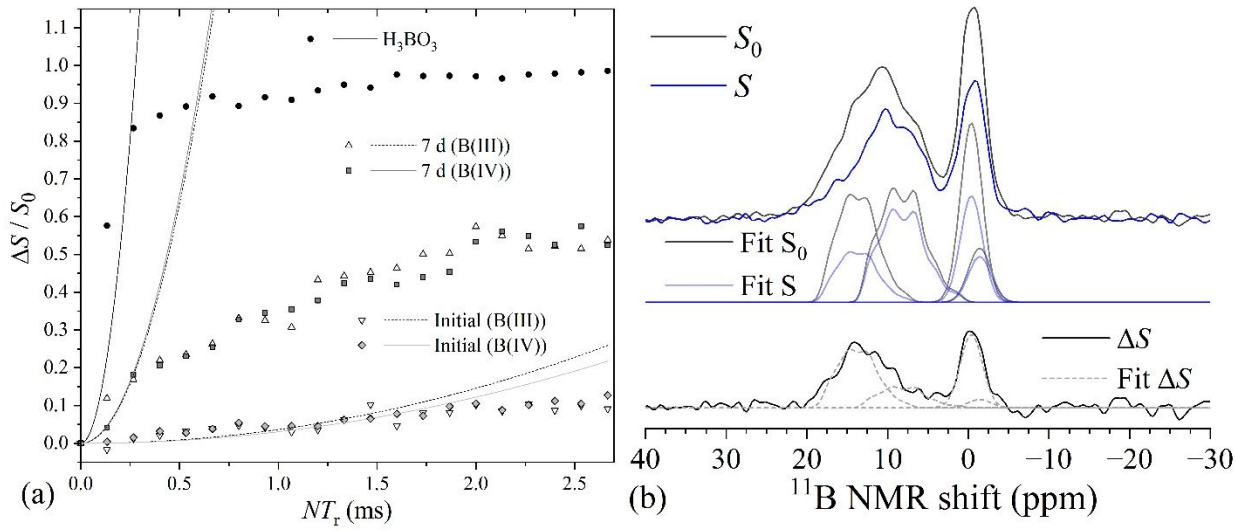

Figure 6. (a) $^{11}B\{^{1}H\}$ REDOR curves and parabolic fits of the initial dephasing behavior obtained for the unexposed (initial) and exposed (7 d) PB2-P3 glass samples, and the model compound $B(OH)_3$. (b) S_0, S, and ΔS spectra of the exposed glass sample (7 d), obtained by co-adding six spectra from the REDOR curve centered around a dipolar mixing time of 1.07 ms (the 8th point), and simplified spectral deconvolutions highlighting the different dephasing behavior of the boron species represented by the assumed lineshape components. The following lineshape parameters were used for the deconvolutions: B(III)-a: C_Q = 2.5 MHz, η_Q = 0.5, δ_{cs}^{iso} = 18.2 ppm; B(III)-b: C_Q = 2.7 MHz, η_Q = 0.5, δ_{cs}^{iso} = 13.3 ppm; B(IV)-a,c: Gaussian, δ_{cs}^{iso} = -0.4 ppm, FWHM = 620 Hz; B(IV)-b,c: Gaussian δ_{cs}^{iso} = -1.4 ppm, FWHM = 640 Hz.

In an attempt to probe the phosphate species both in the bulk of the glass and near the surface of the Tris-exposed glasses, ^{31}P MAS NMR and $^{1}H \rightarrow ^{31}P$ CP-MAS NMR were performed on selected samples. Comparisons between single resonance and CP-MAS spectra are displayed in Figure 7a-c for PB2-P5, MB2-P5, and PA2-P3 samples dissolved for 1 day, 3 days, and 7 days, respectively, as compared to the initial glass spectra. The fitted deconvolutions of ^{31}P MAS NMR spectra are also depicted; the fitting parameters are listed in Table S3. In our previous publication,[35] several species were identified within the region 3 to -19 ppm associated with P^0, P^1, P^2, and P^3 units, with or without P–O–B linkages. The fits displayed in Figure 7a-c were guided by the fitting parameters as reported in our previous article,[35] maintaining similar FWHM and isotropic chemical shift values. In the studied samples exposed to Tris-HNO_3, the most notable changes occurring in the spectra are a slight sharpening of the P^1_{1P} (P^1 species linked to another P, labeled P^1_{1P}-a)

resonance near 6 ppm, and the development of a minor, sharp secondary peak near 3 ppm (labeled $P^1{}_{1P}$-b in Table S3). These peaks indicate the possible development of more highly-ordered P^1 species as a result of dissolution processes. Further, a quantitative picture of the overall spectral changes occurring following Tris-HNO_3 exposure (depicted in Table S3) indicates that $<n_P>$, the average number of bridging oxygen species around phosphorus, increases for each glass studied in the exposed samples (relative to the unexposed ones), and $<m_B(P)>$, the average number of B neighbors around P, also tends to increase. This finding indicates that less connected phosphate units (such as P^0 units) are more easily leached from the glass while species connected to one or more B or P are more effectively retained in the glassy network. The $^1H \rightarrow {}^{31}P$ CP-MAS NMR spectra recorded for selective detection of those phosphate species interacting with the hydrous species near the surface are displayed in Figure 7a-c. While these spectra generally show the signals in similar locations as the single resonance spectra, there are two notable changes; the sharp signal near 3 ppm attributed to the $P^1{}_{1P}$-b species appears enhanced, identifying it as a surface species. Secondly, a broader feature that is visibly enhanced compared to the single-pulse spectra emerges near -3 ppm. To further examine this, Figure 7d presents the CP-MAS spectra of the PB2-P5 sample dissolved for 1 day as examined using variable cross-polarization contact times, in an attempt to differentiate the strength of internuclear $^1H/^{31}P$ interactions for distinct phosphate species. While short-contact time experiments emphasize phosphate species closest to protons, at longer contact times, phosphate species that are more distant to protons are also being detected due to spin diffusion processes. These variable contact time experiments also indicate the particularly close proximity of the $P^1{}_{1P}$-b species (sharp line at 3 ppm) and the P–O–B(IV) species giving rise to the broader signal near -3 ppm to protons, confirming their nature as surface species with close proton contacts.

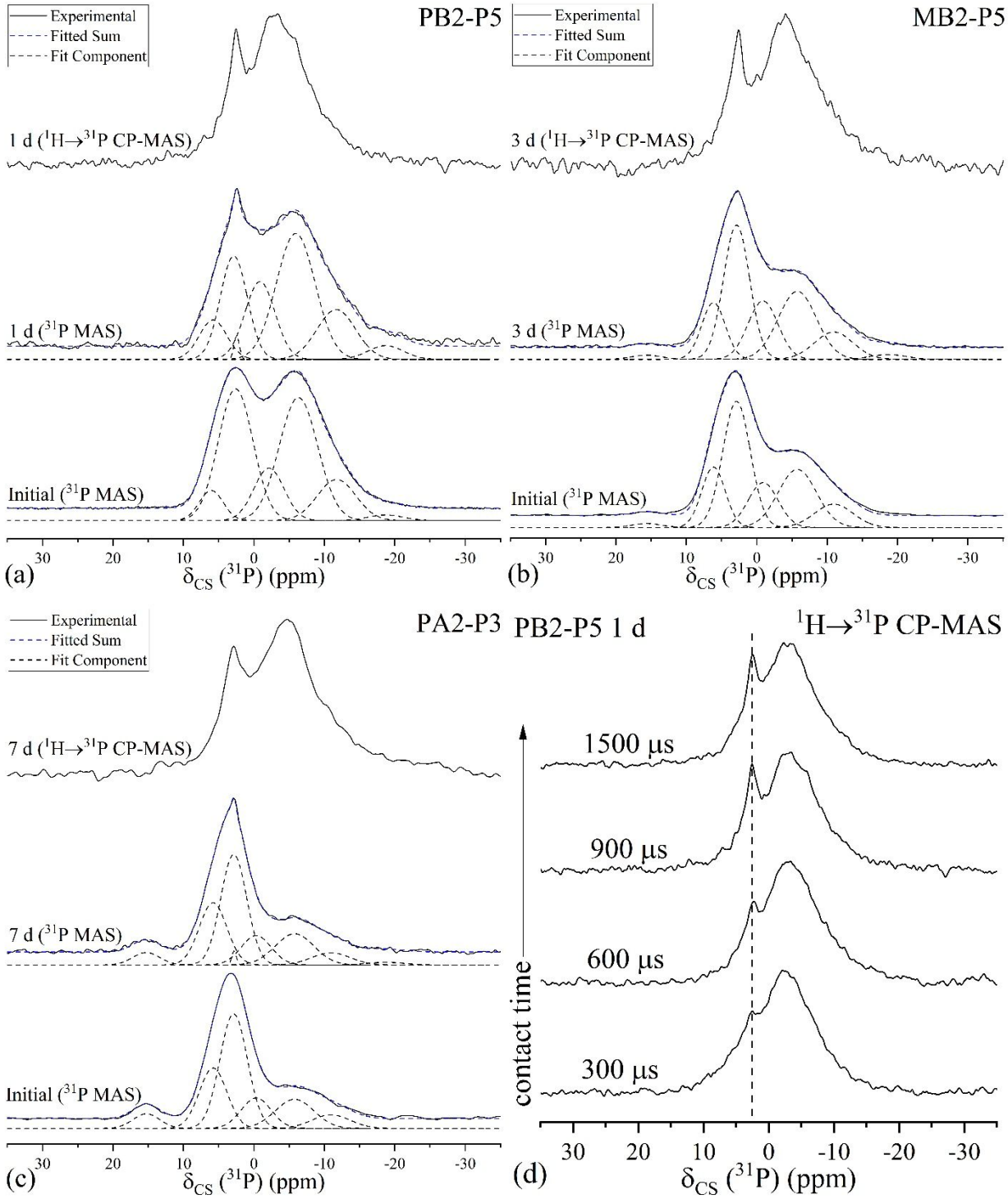

Figure 7. ^{31}P MAS NMR spectra for the as-synthesized (a) PB2-P5, (b) MB2-P5, and (c) PA2-P3 samples, as compared to the ^{31}P MAS NMR and ^{1}H→^{31}P CP-MAS NMR spectra of analogous glass powders subjected to 1-, 3-, and 7- day degradation experiments, respectively, in Tris-HNO_3 environments. Lineshape fittings of all the ^{31}P MAS NMR spectra are also displayed. (d) depicts

the $^{1}H \rightarrow ^{31}P$ CP-MAS NMR spectrum of the PB5 1-day sample as analyzed using different $^{1}H \rightarrow ^{31}P$ contact times.

To further explore the structure of hydrated layers formed on the glass surface, 14-day recovered MB0, MB2-P5, and PB2-P5 samples were analyzed by ^{29}Si MAS NMR (Figure 8a) and $^{1}H \rightarrow ^{29}Si$ CP-MAS NMR (Figure 8b). According to the ^{29}Si MAS NMR results from our previous study,[35] the silicate network in the analyzed (unexposed) samples comprised at least 67% Si^4 with the remainder of the inventory being Si^3 units before dissolution in Tris-HNO_3. After exposure to Tris-HNO_3, the ^{29}Si MAS NMR spectra show the following three main resonances: -91 ppm (Si^2), -101 ppm (Si^3), and -111 ppm (Si^4). The former two species likely represent silicate species containing hydroxyl groups: Si^2-$(OH)_2$ and Si^3-OH, respectively, whereas the latter represents fully connected silicate species that are cross-polarized from more remote protons across longer ^{1}H-^{29}Si distances. The relative fraction of these species can be estimated from the fitted single-pulse ^{29}Si MAS NMR spectra of these samples (displayed in Figure 8a); the fitting parameters and fractions of each species are depicted in Table S4. As expected, the results indicate that Tris-exposure leads to some depolymerization of the silicate network and reduced the average silicate polymerization in studied samples, through either Na^+/H^+ ion exchange with NBO sites or silica hydrolysis.

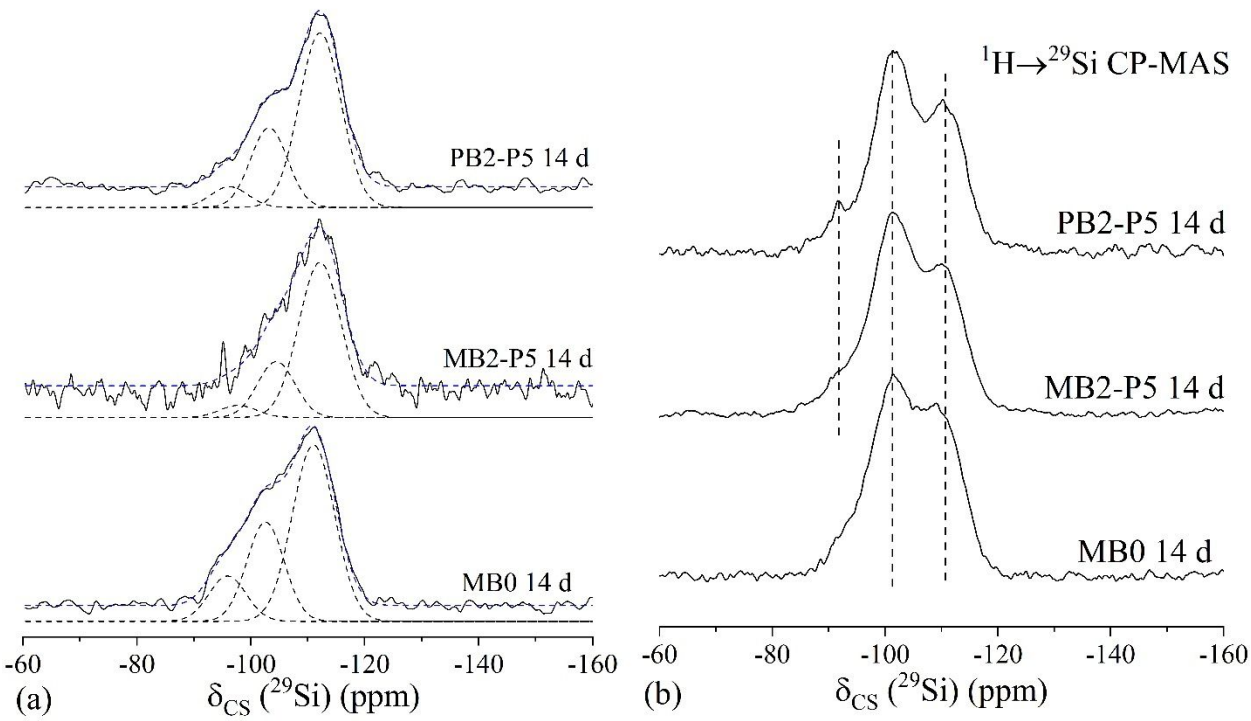

Figure 8. (a) ^{29}Si MAS NMR and (b) ^{1}H→^{29}Si CP-MAS NMR spectra of selected samples recovered from 14-day experiments in Tris-HNO_3 solutions. Lineshape fittings of ^{29}Si MAS NMR spectra are also displayed in (a).

5.5 Glass surface evolution during degradation experiments

In addition to the degradation experiments performed on glass powders, two monolithic polished coupons each for PB2-P5 and MB2-P5 glasses were studied for their degradation behavior in Tris-HNO_3 for 3-day and 7-day durations. Both polished (undissolved) and dissolved samples were analyzed for their surface characteristics using XPS and ERDA analyses, whereas the cross-section of the PB2-P5 sample recovered from 7 days of glass degradation experiments was analyzed using SEM-EDS to decipher the microstructure of the hydrated surface layers.

Table 5 presents a comparison between the surface chemistry (3-10 nm probe depth) of the polished monolithic glass samples/coupons (PB2-P5 and MB2-P5) and those dissolved/corroded in Tris-HNO_3 for 3 and 7 days, respectively. Further, the surface chemistry of the polished samples has also been compared with their bulk compositions, as analyzed by ICP-OES. Overall, the

comparison between the surface and bulk chemistry of the investigated glasses is within ±1 %. However, a slightly higher deviation of 2-4 % in the surface concentrations of B (depleted) and O (enriched), as compared to the bulk, has been observed. Upon 3 days of exposure to Tris-HNO_3, both glasses displayed a nearly complete dissolution of P and B from the top surface, coupled with a >85 % reduction in Na content. Likewise, 7-day samples were entirely depleted in P and B, while showing similar amounts of Na remaining in the surface layers. Thus, the remaining surface layers are primarily O and Si, with a stoichiometry ~3:1 (O:Si), which is a much higher ratio than observed in pure SiO_2. This deviation from stoichiometry indicates a significantly depolymerized silicate layer at the surface, consistent with the high concentrations of Si^2-$(OH)_2$ and Si^3-OH units detected by NMR.

Table 5. Surface compositions of PB2-P5 and MB2-P5 samples as measured in the top 3–10 nm layer via XPS analysis (atomic percentages accurate within ±5%). In each sample, we have compared compositions of polished and corroded samples to the bulk compositions measured using ICP-OES. H concentrations were measured using ERDA analysis.

Element (at. % by XPS)	**Sample**							
	PB2-P5				**MB2-P5**			
	Bulk	**Polished Surface**	**3 d**	**7 d**	**Bulk**	**Polished Surface**	**3 d**	**7 d**
Na	13.7	13.9	1.9	1.9	13.4	13.2	1.2	1.1
P	2.6	2.1	0.2	0.0	2.7	2.0	0.0	0.0
B	15.4	13.3	0.9	1.4	13.0	11.8	0.0	0.0
Si	10.6	9.5	21.9	22.4	12.6	11.5	24.0	23.0
O	57.7	61.3	75.2	74.3	58.2	61.5	74.9	75.8
H*	--	<0.1	n.d.‡	10.2	--	<0.1	6.5	6.8

*H concentration in the top ~350 nm as determined from ERDA (within ±5 %)
‡Not determined

Furthermore, the hydrogen content in the surface layers of these glass samples has been measured by ERDA, and the spectra are displayed in Figure 9, while Table 5 presents the calculated hydrogen contents. ERDA, which probes a significantly larger depth of the surface (~350 nm), indicates that H content is higher in the exposed PB2-P5 sample (10.2%) as compared to the exposed MB2-P5 samples (6.5-6.8%). The PB2-P5 3-day sample was not examined using

ERDA due to the complete removal of the brittle surface layer upon sample handling. The elevation in hydrogen content in the surface layers of PB2-P5 in comparison to MB2-P5 glass may be explained from a standpoint of elemental release since PB glasses exhibit faster dissolution kinetics / NL curves in comparison to MB glasses. Accordingly, it can be expected that protons and water molecules can diffuse more extensively into the glass surface for the PB2-P5 glass.

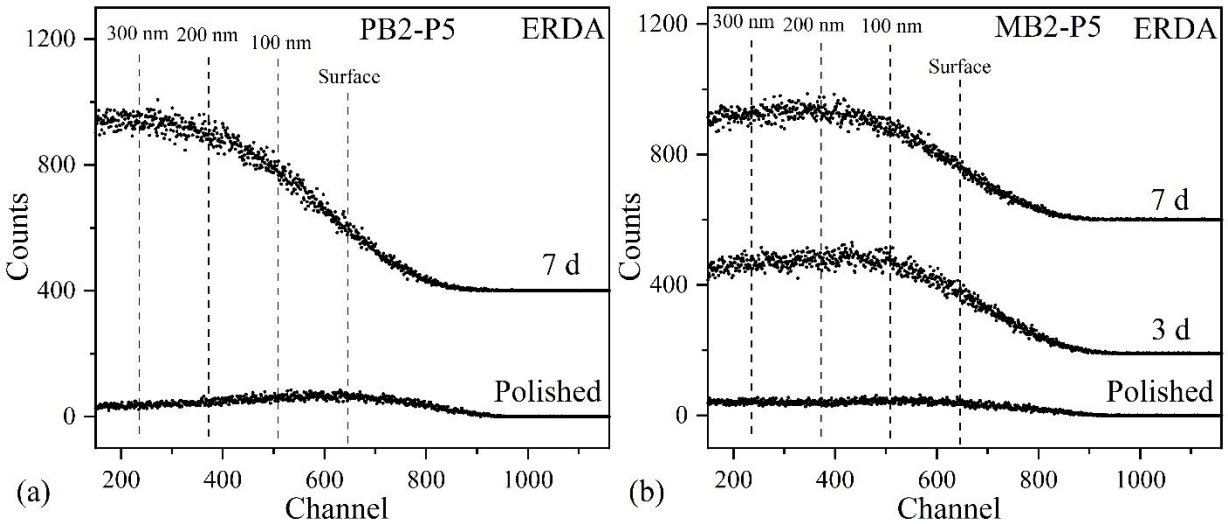

Figure 9. ERDA spectra of (a) PB2-P5 and (b) MB2-P5 polished glass coupons subjected to 3- and 7- day degradation experiments in Tris-HNO_3 solutions.

The cross-sectional SEM and EDS analysis of the PB2-P5 glass dissolved for 7 days has been performed to probe the entire depth of hydrated glass layers, to supplement the XPS and ERDA studies of the top surface layers. In this way, it is possible to understand the entire interface between the pristine glass and the fluid, including the reactive interface alongside the established hydrated layers. Accordingly, Figure 10 displays SEM images and EDS maps of the glass' cross-section. Figures 10a and b contain three regions, labeled 'g' for pristine glass, 'h' for hydrated layer, and 'e' for epoxy resin. It is evident from these images that the thickness of the fully hydrated layer varies between 150 and 200 μm, thus, it is orders of magnitude larger than the probe depth of either XPS or ERDA. Additionally, this layer is observed to undergo thickness fluctuation and

reveals significant cracking behavior, where many of the propagated cracks are perpendicular to the interface between the pristine glass and the hydrated layer. The presence of cracking throughout this layer is consistent with our observations of apparent brittleness in the surface layers, which may indicate weak bonding to the pristine glass surface and/or weakly bound silicate species. To verify the composition of this layer, Figure 10c displays the EDS maps in this region, which confirms that although the pristine glass layers consist of Na, P, Si, and O, the hydrated layer exclusively contains Si and O (in the absence of Na and P), agreeing with the findings from XPS in the top 3-10 nm of the surface. It should be noted that although B content is not readily detectable in EDS maps due to its low K_{α} energy, the ^{11}B MAS NMR results previously discussed, suggest that certain B species are likely also contained within the gel layer.

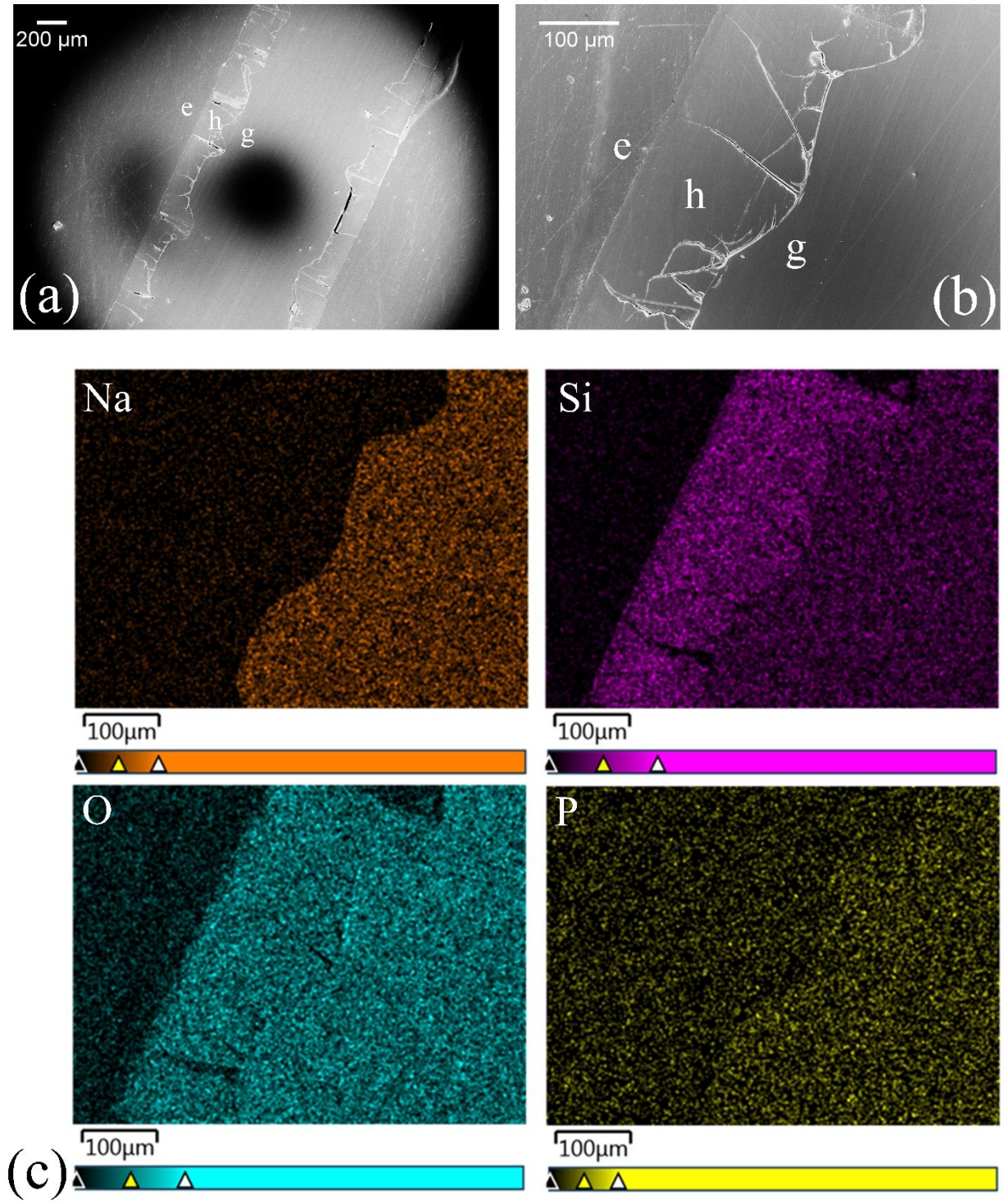

Figure 10. SEM images of the cross-section of the PB2-P5 glass subjected to 7-day degradation experiments (taken in secondary electron mode), at (a) 100- and (b) 500-fold magnification. (c) displays the EDS maps of the region depicted in the SEM image of (b).

6. Discussion

With an overarching goal of proposing a rational design of borosilicate-based bioactive glasses with tunable dissolution behavior and controlled ionic release for soft tissue repair and regeneration, the present study is aimed at unearthing the underlying compositional and structural drivers governing the degradation behavior of borosilicate-based model bioactive glasses. In this context, the results presented here reveal that, in general, two compositional parameters, i.e., *R* (Na_2O/B_2O_3) and *K* (SiO_2/B_2O_3), should be thoughtfully considered when designing a glass with controlled degradation rates *in vitro* or *in vivo*. These ratios not only impact the glass network constitution, but also significantly influence the short- and medium-range ordering in the structure, including features such as boron coordination, borate/silicate network connectivity, and overall network polymerization, each of which exhibits a significant impact on the reactivity of the glass in physiological fluids. For instance, it has been shown that the degradation rates are inversely proportional to *R* and *K* (as displayed in Figure 3a), in the order: peralkaline ($R = 1.25$, $K = 2.75$) < metaboric ($R = 1$, $K = 2$) < perboric ($R = 0.83$, $K = 1.5$). These kinetic differences in the baseline glasses (P_2O_5-free) can be explained by a change in the borosilicate network makeup since boron species are known to undergo hydrolysis and release from the glass at significantly elevated rates in comparison to silicate units.[57] Specifically, the overall rates of elemental release vary by at least a factor of two when comparing the extremes in the peralkaline and perboric systems. Thus, carefully tuning the *R* and *K* ratios during glass compositional design allows for the development of glasses with controlled functional ion release within the studied region. With decreasing *R* and *K*, the fractional contribution of B–O–B linkages to the network increases. As the quantum chemical calculations mentioned above indicate that such linkages are hydrolytically less stable

than Si–O–B or Si–O–Si linkages, it is easy to understand that the highest hydrolysis rates are observed in the perboric glass system.

Further, the modification of the glass' hydrolytic properties is then effected upon by the addition of P_2O_5. In the most rapidly hydrolyzing perboric system, its impact upon glass degradation turns out to be minor, whereas degradation rates reduce by up to 20-35 % in metaboric and peralkaline glasses as a result of 3-5 mol. % of P_2O_5 addition. At the structural level, the addition of P_2O_5 into the glass increases the polymerization in the silicate network and decreases the fraction of four-coordinated borate units due to the re-distribution of Na^+ towards phosphate units. In addition, stepwise additions of P_2O_5 also result in increased P–O–B(IV) linking at the expense of isolated phosphate units. In the studied systems, since *R* and *K* ratios are maintained while substituting P_2O_5, the direct structural impacts upon degradation behavior can be uncovered within each glass series. As expected, the ^{11}B MAS NMR experiments confirm that B(III) species are preferentially extracted in comparison to B(IV) species, as evidenced from the significant reductions in B(III) fraction in the post-dissolution glasses, but to the largest extent in glasses undergoing greater magnitudes of elemental release. Furthermore, it is confirmed that ion-exchange/hydrolysis reactions of Na, P, B, and to a lesser extent, Si units in the glass result in a silicate-rich gel layer on the glass surface which contains higher concentrations of Si^2 and Si^3 units with terminal hydroxyl groups. Phosphate species, on the other hand, are not detected to undergo preferential extraction. However, based on our observations from ^{11}B MAS NMR, it can be hypothesized that P–O–B(IV) linked units, which dominate the speciation at higher P_2O_5-contents,[35] dissolve at a slower pace as compared to isolated phosphate species. Based on our findings and the known literature,[23, 85-92] it can be concluded that the presence of high concentrations of B(III), isolated P^0/P^1, and Si^2/Si^3 (specifically, NBO sites) species in the glass

structure result in a faster degradation and ion release rates. On the other hand, the presence of B(IV), P^2/P^3 (P–O–B(IV)), and Si^4 species tend to slow down the degradation behavior of borosilicate glasses.

Thus, to rationalize our findings within each compositional regime, the overall dissolution rate is governed by a delicate balance between the structure and chemistry of glasses. For example, the perboric glasses exhibit minimal changes in degradation rates as a function of P_2O_5 content, since the B(III) fractions (and B_2O_3 content) are higher and rise with P_2O_5 content, thus, more effectively balancing out the effects of increasing Si^4 and P–O–B(IV) units. Further, as *R* and *K* decrease (i.e., in metabolic and peralkaline glasses), the drop in B(III) fraction (and B_2O_3 content) results in degradation rates which are more significantly controlled by the rises in Si^4 and P–O–B(IV) linkages, thus causing an overall rate decrease upon increasing P_2O_5 content. It is expected that the comprehensive structural understanding of the degradation behavior in the sodium borosilicate and phospho-borosilicate glass systems presented here will promote a rational design of borosilicate-based bioactive glasses with the desired degradation rates and ionic release profiles tailored for the repair and regeneration of specific hard/soft tissues.

7. Conclusions

Using a systematic and dedicated approach, the present study explored the compositional and structural drivers controlling the degradation behavior of borosilicate-based model bioactive glasses (in pH = 7.4) across a broad composition space, including perboric (Na/B < 1), metaboric (Na/B = 1), and peralkaline (Na/B > 1) regimes. A multi-scale investigation employing a suite of state-of-the-art characterization techniques reveals that the kinetics of glass degradation depends on the *R* (Na_2O/B_2O_3) and *K* (SiO_2/B_2O_3) ratios, reflecting the details of the short- and

intermediate-range molecular structure controlling the ionic release rates. Successive additions of P_2O_5 into sodium borosilicate glasses result in complex glass structural changes that impact degradation behavior due to multiple factors. The observed degradation behavior can be explained from the viewpoint of the effect that specific NFUs (*i.e.*, B(III)/B(IV), Si^3/Si^4, etc.) have upon ionic release behavior, through the formation of oxygen linkages and interactions with Na^+. The present study illustrates that a comprehensive understanding of the composition-structure-property relationships can facilitate the development of novel borosilicate bioactive glasses with tunable degradation and ionic release rates specific for targeted applications in soft tissue engineering.

Conflicts of interest

The authors confirm the absence of any conflict of interest with this submission.

Acknowledgments

This material is based upon work supported by the National Science Foundation under Grant No. 1507131 and 2034871. The support of the Centers for Global Advancement and International Affairs (GAIA) at Rutgers University is acknowledged. H.E. and H.B. thank FAPESP for support under Grant No. 2013/07793-6. H.B. also thanks for post-doctoral support received from FAPESP (grant number 2019/26399-3) and from the Deutsche Forschungsgemeinschaft. The authors also thank the Characterization Sciences group at Corning Incorporated for the compositional analysis of the glasses.

References

(1) Balasubramanian, P.; Buettner, T.; Miguez Pacheco, V.; Boccaccini, A. R. Boron-containing bioactive glasses in bone and soft tissue engineering. *J. Euro. Ceram. Soc.* **2018**, *38* (3), 855-869.
(2) Balasubramanian, P.; Hupa, L.; Jokic, B.; Detsch, R.; Grünewald, A.; Boccaccini, A. R. Angiogenic potential of boron-containing bioactive glasses: in vitro study. *J. Mater. Sci.* **2017**, *52* (15), 8785-8792.
(3) Kargozar, S.; Baino, F.; Hamzehlou, S.; Hill, R. G.; Mozafari, M. Bioactive glasses: sprouting angiogenesis in tissue engineering. *Trends Biotechnol.* **2018**, *36* (4), 430-444.
(4) Baino, F.; Novajra, G.; Miguez Pacheco, V.; Boccaccini, A. R.; Vitale-Brovarone, C. Bioactive glasses: Special applications outside the skeletal system. *J. Non. Cryst. Solids* **2016**, *432*, 15-30.
(5) Miguez Pacheco, V.; Hench, L. L.; Boccaccini, A. R. Bioactive glasses beyond bone and teeth: Emerging applications in contact with soft tissues. *Acta Biomater.* **2015**, *13*, 1-15.
(6) Lin, Y. N.; Brown, R. F.; Jung, S. B.; Day, D. E. Angiogenic effects of borate glass microfibers in a rodent model. *J. Biomed. Mater. Res. A* **2014**, *102* (12), 4491-4499.
(7) Kargozar, S.; Hamzehlou, S.; Baino, F. Potential of bioactive glasses for cardiac and pulmonary tissue engineering. *Materials* **2017**, *10* (12), 1429.
(8) Kargozar, S.; Singh, R. K.; Kim, H.-W.; Baino, F. "Hard" ceramics for "Soft" tissue engineering: Paradox or opportunity? *Acta Biomater.* **2020**, *115*, 1-28.
(9) Souza, M. T.; Peitl, O.; Zanotto, E. D.; Boccaccini, A. R. Novel double-layered conduit containing highly bioactive glass fibers for potential nerve guide application. *Int. J. Appl. Glass Sci.* **2016**, *7* (2), 183-194.
(10) Koudehi, M. F.; Fooladi, A. A. I.; Mansoori, K.; Jamalpoor, Z.; Amiri, A.; Nourani, M. R. Preparation and evaluation of novel nano-bioglass/gelatin conduit for peripheral nerve regeneration. *J. Mater. Sci. Mater. Med.* **2014**, *25* (2), 363-373.
(11) Bunting, S.; Di Silvio, L.; Deb, S.; Hall, S. Bioresorbable glass fibres facilitate peripheral nerve regeneration. *J. Hand Surg. Eur. Vol.* **2005**, *30* (3), 242-247.
(12) Kargozar, S.; Mozafari, M.; Ghenaatgar-Kasbi, M.; Baino, F. Bioactive glasses and glass/polymer composites for neuroregeneration: should we be hopeful? *Appl. Sci.* **2020**, *10* (10), 3421.
(13) Marquardt, L. M.; Day, D.; Sakiyama-Elbert, S. E.; Harkins, A. B. Effects of borate-based bioactive glass on neuron viability and neurite extension. *J. Biomed. Mater. Res. A* **2014**, *102* (8), 2767-2775.
(14) Gupta, B.; Papke, J. B.; Mohammadkhah, A.; Day, D. E.; Harkins, A. B. Effects of chemically doped bioactive borate glass on neuron regrowth and regeneration. *Ann. Biomed. Eng.* **2016**, *44* (12), 3468-3477.
(15) Jia, W.; Hu, H.; Li, A.; Deng, H.; Hogue, C. L.; Mauro, J. C.; Zhang, C.; Fu, Q. Glass-activated regeneration of volumetric muscle loss. *Acta Biomater.* **2020**, *103*, 306-317.
(16) Rahaman, M. N.; Day, D. E.; Bal, B. S.; Fu, Q.; Jung, S. B.; Bonewald, L. F.; Tomsia, A. P. Bioactive glass in tissue engineering. *Acta Biomater.* **2011**, *7* (6), 2355-2373.
(17) Hamilton, G.; Seidman, R. A comparison of the recovery period for women and men after an acute myocardial infarction. *Heart Lung* **1993**, *22* (4), 308-315.
(18) Bigger Jr, J. T.; Fleiss, J. L.; Rolnitzky, L. M.; Steinman, R. C.; Schneider, W. J. Time course of recovery of heart period variability after myocardial infarction. *J. Am. Coll. Cardiol.* **1991**, *18* (7), 1643-1649.
(19) Chen, Q.; Jin, L.; Cook, W. D.; Mohn, D.; Lagerqvist, E. L.; Elliott, D. A.; Haynes, J. M.; Boyd, N.; Stark, W. J.; Pouton, C. W. Elastomeric nanocomposites as cell delivery vehicles and cardiac support devices. *Soft Matter* **2010**, *6* (19), 4715-4726.
(20) George, J. L.; Brow, R. K. In-situ characterization of borate glass dissolution kinetics by μ-Raman spectroscopy. *J. Non. Cryst. Solids* **2015**, *426*, 116-124.
(21) Jung, S. B.; Day, D. E.; Day, T.; Stoecker, W.; Taylor, P. Treatment of non-healing diabetic venous stasis ulcers with bioactive glass. *Wound Repair Regen.* **2011**, *19* (2), A30.
(22) Naseri, S.; Lepry, W. C.; Nazhat, S. N. Bioactive glasses in wound healing: hope or hype? *J. Mater. Chem. B* **2017**, *5* (31), 6167-6174.

(23) Kapoor, S.; Youngman, R. E.; Zakharchuk, K.; Yaremchenko, A.; Smith, N. J.; Goel, A. Structural and Chemical Approach toward Understanding the Aqueous Corrosion of Sodium Aluminoborate Glasses. *J. Phys. Chem. B* **2018**, *122* (48), 10913-10927.
(24) Bitar, M.; Salih, V.; Mudera, V.; Knowles, J. C.; Lewis, M. P. Soluble phosphate glasses: in vitro studies using human cells of hard and soft tissue origin. *Biomaterials* **2004**, *25* (12), 2283-2292.
(25) Liu, X.; Rahaman, M. N.; Day, D. E. Conversion of melt-derived microfibrous borate (13-93B3) and silicate (45S5) bioactive glass in a simulated body fluid. *J. Mater. Sci. Mater. Med.* **2013**, *24* (3), 583-595.
(26) Schoen, F. J.; Levy, R. J.; Tam, H.; Vyavahare, N. 2.4.5 - Pathological Calcification of Biomaterials. In *Biomaterials Science*, Fourth Edition; Wagner, W. R.; Sakiyama-Elbert, S. E.; Zhang, G.; Yaszemski, M. J., Eds.; Academic Press, 2020; pp 973-994.
(27) Mosier, J.; Nguyen, N.; Parker, K.; Simpson, C. L. Calcification of Biomaterials and Diseased States. In *Biomaterials-Physics and Chemistry*, New Addition; Pignatello, R.; Musumeci, T., Eds.; IntechOpen, 2017.
(28) Proudfoot, D. Calcium signaling and tissue calcification. *Cold Spring Harb. Perspect. Biol.* **2019**, *11* (10), a035303.
(29) Ohnishi, M.; Nakatani, T.; Lanske, B.; Razzaque, M. S. In vivo genetic evidence for suppressing vascular and soft-tissue calcification through the reduction of serum phosphate levels, even in the presence of high serum calcium and 1, 25-dihydroxyvitamin d levels. *Circ. Cardiovasc. Genet.* **2009**, *2* (6), 583-590.
(30) Jowsey, J.; Balasubramaniam, P. Effect of phosphate supplements on soft-tissue calcification and bone turnover. *Clin. Sci.* **1972**, *42* (3), 289-299.
(31) Yun, Y. H.; Bray, P. J. Nuclear magnetic resonance studies of the glasses in the system Na_2O-B_2O_3-SiO_2. *J. Non. Cryst. Solids* **1978**, *27* (3), 363-380.
(32) Dell, W. J.; Bray, P. J.; Xiao, S. Z. ^{11}B NMR studies and structural modeling of Na_2O-B_2O_3-SiO_2 glasses of high soda content. *J. Non. Cryst. Solids* **1983**, *58* (1), 1-16.
(33) Manara, D.; Grandjean, A.; Neuville, D. R. Structure of borosilicate glasses and melts: A revision of the Yun, Bray and Dell model. *J. Non. Cryst. Solids* **2009**, *355* (50–51), 2528-2531.
(34) van Wüllen, L.; Müller-Warmuth, W.; Papageorgiou, D.; Pentinghaus, H. J. Characterization and structural developments of gel-derived borosilicate glasses: a multinuclear MAS-NMR study. *J. Non. Cryst. Solids* **1994**, *171* (1), 53-67.
(35) Stone-Weiss, N.; Bradtmüller, H.; Fortino, M.; Bertani, M.; Youngman, R. E.; Pedone, A.; Eckert, H.; Goel, A. Combined Experimental and Computational Approach toward the Structural Design of Borosilicate-Based Bioactive Glasses. *J. Phys. Chem. C* **2020**, 124 (32), 17655-17674.
(36) Tainio, J.; Salazar, D. A.; Nommeots-Nomm, A.; Roiland, C.; Bureau, B.; Neuville, D.; Brauer, D.; Massera, J. Structure and in vitro dissolution of Mg and Sr containing borosilicate bioactive glasses for bone tissue engineering. *J. Non. Cryst. Solids* **2020**, *533*, 119893.
(37) Wang, H.; Zhao, S.; Xiao, W.; Xue, J.; Shen, Y.; Zhou, J.; Huang, W.; Rahaman, M. N.; Zhang, C.; Wang, D. Influence of Cu doping in borosilicate bioactive glass and the properties of its derived scaffolds. *Mater. Sci. Eng. C* **2016**, *58*, 194-203.
(38) Deng, Z.; Lin, B.; Jiang, Z.; Huang, W.; Li, J.; Zeng, X.; Wang, H.; Wang, D.; Zhang, Y. Hypoxia-mimicking cobalt-doped borosilicate bioactive glass scaffolds with enhanced angiogenic and osteogenic capacity for bone regeneration. *Int. J. Biol. Sci.* **2019**, *15* (6), 1113.
(39) Ter Braake, A. D.; Tinnemans, P. T.; Shanahan, C. M.; Hoenderop, J. G. J.; de Baaij, J. H. F. Magnesium prevents vascular calcification in vitro by inhibition of hydroxyapatite crystal formation. *Sci. Rep.* **2018**, *8* (1), 1-11.
(40) Stone-Weiss, N.; Pierce, E. M.; Youngman, R. E.; Gulbiten, O.; Smith, N. J.; Du, J.; Goel, A. Understanding the structural drivers governing glass–water interactions in borosilicate based model bioactive glasses. *Acta Biomater.* **2018**, *65*, 436-449.
(41) El-Kady, A. M.; Ali, A.; El-Fiqi, A. Controlled delivery of therapeutic ions and antibiotic drug of novel alginate-agarose matrix incorporating selenium-modified borosilicate glass designed for chronic wound healing. *J. Non. Cryst. Solids* **2020**, *534*, 119889.

(42) Wu, C.; Zhang, Z.; Zhou, K.; Chen, W.; Tao, J.; Li, C.; Xin, H.; Song, Y.; Ai, F. Preparation and characterization of borosilicate-bioglass-incorporated sodium alginate composite wound dressing for accelerated full-thickness skin wound healing. *Biomed. Mater.* **2020**, *15* (5), 055009.
(43) Jeznach, O.; Gajc, M.; Korzeb, K.; Kłos, A.; Orliński, K.; Stępień, R.; Krok-Borkowicz, M.; Rumian, Ł.; Pietryga, K.; Reczyńska, K. New calcium-free $Na_2O–Al_2O_3–P_2O_5$ bioactive glasses with potential applications in bone tissue engineering. *J. Am. Ceram. Soc.* **2018**, *101* (2), 602-611.
(44) Wu, C. T.; Fan, W.; Gelinsky, M.; Xiao, Y.; Simon, P.; Schulze, R.; Doert, T.; Luo, Y. X.; Cuniberti, G. Bioactive $SrO-SiO_2$ glass with well-ordered mesopores: Characterization, physiochemistry and biological properties. *Acta Biomater.* **2011**, *7* (4), 1797-1806.
(45) Magyari, K.; Stefan, R.; Vulpoi, A.; Baia, L. Bioactivity evolution of calcium-free borophosphate glass with addition of titanium dioxide. *J. Non. Cryst. Solids* **2015**, *410*, 112-117.
(46) Magyari, K.; Stefan, R.; Vodnar, D. C.; Vulpoi, A.; Baia, L. The silver influence on the structure and antibacterial properties of the bioactive $10B_2O_3−30Na_2O−60P_2O_5$ glass. *J. Non. Cryst. Solids* **2014**, *402*, 182-186.
(47) Baino, F.; Hamzehlou, S.; Kargozar, S. Bioactive glasses: where are we and where are we going? *J. Funct. Biomater.* **2018**, *9* (1), 25.
(48) Lin, Y.; McKinnon, K. E.; Ha, S. W.; Beck Jr, G. R. Inorganic phosphate induces cancer cell mediated angiogenesis dependent on forkhead box protein C2 (FOXC2) regulated osteopontin expression. *Mol. Carcinog.* **2015**, *54* (9), 926-934.
(49) Camalier, C. E.; Yi, M.; Yu, L. R.; Hood, B. L.; Conrads, K. A.; Lee, Y. J.; Lin, Y.; Garneys, L. M.; Bouloux, G. F.; Young, M. R. An integrated understanding of the physiological response to elevated extracellular phosphate. *J. Cell. Physiol.* **2013**, *228* (7), 1536-1550.
(50) Wang, F.; Balasubramanya, N.; Qin, Q.; Youngman, R. E.; Mukherjee, P.; Stone-Weiss, N.; Goel, A. Multiscale Investigation of the Mechanisms Controlling the Corrosion of Borosilicate Glasses in Hyper-Alkaline Media. *J. Phys. Chem. C* **2020**, *124* (50), 27542-27557.
(51) International Standard. Biological evaluation of medical devices. Part 14: Identification and quantification of degradation products from ceramics. In: *ISO 10993-14*; 2001.
(52) Stone-Weiss, N.; Smith, N. J.; Youngman, R. E.; Pierce, E. M.; Goel, A. Dissolution kinetics of a sodium borosilicate glass in Tris buffer solutions: Impact of Tris concentration and acid (HCl/HNO_3) identity, Submitted.
(53) Tournié, A.; Majérus, O.; Lefèvre, G.; Rager, M. N.; Walmé, S.; Caurant, D.; Barboux, P. Impact of boron complexation by Tris buffer on the initial dissolution rate of borosilicate glasses. *J. Colloid Interface Sci.* **2013**, *400*, 161-167.
(54) Massiot, D.; Fayon, F.; Capron, M.; King, I.; Le Calvé, S.; Alonso, B.; Durand, J. O.; Bujoli, B.; Gan, Z.; Hoatson, G. Modelling one-and two-dimensional solid-state NMR spectra. *Magn. Reson. Chem.* **2002**, *40* (1), 70-76.
(55) Massiot, D.; Bessada, C.; Coutures, J.; Taulelle, F. A quantitative study of ^{27}Al MAS NMR in crystalline YAG. *J. Magn. Reson.* **1990**, *90* (2), 231-242.
(56) Gullion, T.; Schaefer, J. Rotational-echo double-resonance NMR. *J. Magn. Reson.* **1989**, *81* (1), 196-200.
(57) Stone-Weiss, N.; Youngman, R. E.; Thorpe, R.; Smith, N. J.; Pierce, E. M.; Goel, A. An insight into the corrosion of alkali aluminoborosilicate glasses in acidic environments. *Phys. Chem. Chem. Phys.* **2020**, *22* (4), 1881-1896.
(58) Zielniok, D.; Cramer, C.; Eckert, H. Structure/property correlations in ion-conducting mixed-network former glasses: Solid-state NMR studies of the system $Na_2O-B_2O_3-P_2O_5$. *Chem. Mater.* **2007**, *19* (13), 3162-3170.
(59) Lusvardi, G.; Malavasi, G.; Tarsitano, F.; Menabue, L.; Menziani, M. C.; Pedone, A. Quantitative Structure-Property Relationships of Potentially Bioactive Fluoro Phospho-silicate Glasses. *J. Phys. Chem. B* **2009**, *113* (30), 10331-10338.
(60) Pedone, A.; Chen, X.; Hill, R. G.; Karpukhina, N. Molecular Dynamics Investigation of Halide-Containing Phospho-Silicate Bioactive Glasses. *J. Phys. Chem. B* **2018**, *122* (11), 2940-2948.

(61) Smedskjaer, M. M.; Youngman, R. E.; Striepe, S.; Potuzak, M.; Bauer, U.; Deubener, J.; Behrens, H.; Mauro , J. C.; Yue, Y. Irreversibility of Pressure Induced Boron Speciation Change in Glass. *Sci. Rep.* **2014**, *4*, 3770.
(62) MacDonald, W. M.; Anderson, A.; Schroeder, J. Low-temperature behavior of potassium and sodium silicate glasses. *Phys. Rev. B* **1985**, *31* (2), 1090.
(63) O'Donnell, M.; Watts, S.; Law, R.; Hill, R. Effect of P_2O_5 content in two series of soda lime phosphosilicate glasses on structure and properties–Part II: Physical properties. *J. Non. Cryst. Solids* **2008**, *354* (30), 3561-3566.
(64) Vienna, J. D.; Ryan, J. V.; Gin, S.; Inagaki, Y. Current Understanding and Remaining Challenges in Modeling Long-Term Degradation of Borosilicate Nuclear Waste Glasses. *Int. J. Appl. Glass Sci.* **2013**, *4* (4), 283-294.
(65) Gin, S.; Jollivet, P.; Fournier, M.; Berthon, C.; Wang, Z.; Mitroshkov, A.; Zhu, Z.; Ryan, J. V. The fate of silicon during glass corrosion under alkaline conditions: A mechanistic and kinetic study with the International Simple Glass. *Geochim. Cosmochim. Acta* **2015**, *151*, 68-85.
(66) Kragten, J. Tutorial review. Calculating standard deviations and confidence intervals with a universally applicable spreadsheet technique. *Analyst* **1994**, *119* (10), 2161-2165.
(67) Lu, X.; Deng, L.; Gin, S.; Du, J. Quantitative Structure-Property Relationship (QSPR) Analysis of ZrO2-Containing Soda-Lime Borosilicate Glasses. *J. Phys. Chem. B* **2019**, *123* (6), 1412-1422.
(68) Mascaraque, N.; Bauchy, M.; Smedskjaer, M. M. Correlating the network topology of oxide glasses with their chemical durability. *J. Phys. Chem. B* **2017**, *121* (5), 1139-1147.
(69) Yu, Y.; Eden, M. Structure-composition relationships of bioactive borophosphosilicate glasses probed by multinuclear 11B, 29Si, and 31P solid state NMR. *RSC Adv.* **2016**, *6* (103), 101288-101303.
(70) Ebert, W. L. Comparison of the results of short-term static tests and single-pass flow-through tests with LRM glass (ANL-06/51), Argonne National Laboratory (ANL), 2007.
(71) Gin, S.; Frugier, P.; Jollivet, P.; Bruguier, F.; Curti, E. New Insight into the Residual Rate of Borosilicate Glasses: Effect of S/V and Glass Composition. *Int. J. Appl. Glass Sci.* **2013**, *4* (4), 371-382.
(72) Fournier, M.; Ull, A.; Nicoleau, E.; Inagaki, Y.; Odorico, M.; Frugier, P.; Gin, S. Glass dissolution rate measurement and calculation revisited. *J. Nucl. Mater.* **2016**, *476*, 140-154.
(73) Ebert, W. L. The effects of the glass surface area/solution volume ratio on glass corrosion: a critical review; Argonne National Laboratory, 1995.
(74) Ebert, W. L.; Bates, J. K. A comparison of glass reaction at high and low glass-surface solution volume. *Nucl. Tech.* **1993**, *104* (3), 372-384.
(75) Almeida, R. M.; Pantano, C. G. Structural investigation of silica gel films by infrared spectroscopy. *J. Appl. Phys.* **1990**, *68* (8), 4225-4232.
(76) Abo-Naf, S. M.; El Batal, F. H.; Azooz, M. A. Characterization of some glasses in the system SiO_2, Na_2O•RO by infrared spectroscopy. *Mater. Chem. Phys.* **2003**, *77* (3), 846-852.
(77) Bertoluzza, A.; Fagnano, C.; Morelli, M. A.; Gottardi, V.; Guglielmi, M. Raman and infrared spectra on silica gel evolving toward glass. *J. Non. Cryst. Solids* **1982**, *48* (1), 117-128.
(78) Ferrand, K.; Abdelouas, A.; Grambow, B. Water diffusion in the simulated French nuclear waste glass SON 68 contacting silica rich solutions: Experimental and modeling. *J. Nucl. Mater.* **2006**, *355* (1-3), 54-67.
(79) Doweidar, H.; Saddeek, Y. B. FTIR and ultrasonic investigations on modified bismuth borate glasses. *J. Non. Cryst. Solids* **2009**, *355* (6), 348-354.
(80) Kamitsos, E. I.; Karakassides, M. A.; Chryssikos, G. D. Vibrational-spectra of magnesium-sodium-borate glasses. 2. Raman and mid-infrared investigation of the network structure. *J. Phys. Chem.* **1987**, *91* (5), 1073-1079.
(81) Gin, S.; Neill, L.; Fournier, M.; Frugier, P.; Ducasse, T.; Tribet, M.; Abdelouas, A.; Parruzot, B.; Neeway, J.; Wall, N. The controversial role of inter-diffusion in glass alteration. *Chem. Geol.* **2016**, *440*, 115-123.
(82) Andriambololona, Z.; Godon, N.; Vernaz, E. R717 Glass Alteration in the Presence of Mortar: Effect of the Cement Grade. *Mater. Res. Soc. Symp. Conf. Proc.* **1992**, *257*, 151-158

(83) Mercado-Depierre, S.; Angeli, F.; Frizon, F.; Gin, S. Antagonist effects of calcium on borosilicate glass alteration. *J. Nucl. Mater.* **2013**, *441* (1-3), 402-410.
(84) Du, L.-S.; Stebbins, J. Nature of Silicon−Boron Mixing in Sodium Borosilicate Glasses: A High-Resolution ^{11}B and ^{17}O NMR Study. *J. Phys. Chem. B* **2003**, *107*, 10063-10076.
(85) Brauer, D. S.; Möncke, D. Introduction to the structure of silicate, phosphate and borate glasses. In *Bioactive Glasses*; 2016; pp 61-88.
(86) Abdelghany, A. Novel method for early investigation of bioactivity in different borate bio-glasses. *Spectrochim. Acta A* **2013**, *100*, 120-126.
(87) Tilocca, A.; Cormack, A. N. Structural effects of phosphorus inclusion in bioactive silicate glasses. *J. Phys. Chem. B* **2007**, *111* (51), 14256-14264.
(88) Yu, Y.; Stevensson, B.; Edén, M. Medium-Range Structural Organization of Phosphorus-Bearing Borosilicate Glasses Revealed by Advanced Solid-State NMR Experiments and MD Simulations: Consequences of B/Si Substitutions. *J. Phys. Chem. B* **2017**, *121* (41), 9737-9752.
(89) Stevensson, B.; Yu, Y.; Edén, M. Structure–composition trends in multicomponent borosilicate-based glasses deduced from molecular dynamics simulations with improved B–O and P–O force fields. *Phys. Chem. Chem. Phys.* **2018**, *20* (12), 8192-8209.
(90) Bunker, B. C. Molecular mechanisms for corrosion of silica and silicate glasses. *J. Non. Cryst. Solids Solids* **1994**, *179*, 300-308.
(91) Hamilton, J. P.; Pantano, C. G. Effects of glass structure on the corrosion behavior of sodium-aluminosilicate glasses. *J. Non. Cryst. Solids* **1997**, *222*, 167-174.
(92) Perera, G.; Doremus, R. H. Dissolution Rates of Commercial Soda–Lime and Pyrex Borosilicate Glasses: Influence of Solution pH. *J. Am. Ceram. Soc.* **1991**, *74* (7), 1554-1558.

Figure Captions

Figure 1. (a) T_g vs. P_2O_5 content for PB2-P*x*, MB2-P*x*, and PA2-P*x* glasses and (b) T_g vs. $<n>$, the average network former coordination number, as calculated using equation (2). The dashed line depicts a linear regression fit to the data.

Figure 2. Plots of normalized loss (in units of 10^{-2} mol/m^2) vs. time (hours) for each element present in the glass for (a) PB0, (b) PB2-P5, (c) MB0, (d) MB2-P5, (e) PA0, and (f) PA2-P3.

Figure 3. Degradation rates (in units of 10^{-2} mol·m^{-2}h^{-1}) (a) as a function of P_2O_5 content for Na and B for all glasses in Tris-HNO_3, (b)-I as a function of $<f_B>$ the fraction of B NFU species, and (b)-II as a function of $(<f_B><n_B>) / <n_{B,Mean}>$, the product of $<f_B>$ and $<n_B>$, the average boron connectivity for each glass, scaled by $<n_{B,Mean}>$, the average boron connectivity for all studied compositions, for Na for all glasses in Tris-HNO_3, and (c) for Na, B, and Si for MB2-P*x* glasses in Tris-HCl and Tris-HNO_3 environments.

Figure 4. FTIR spectra of PB2-P5 glass before and after immersion in Tris-HNO_3 for 1 h to 28 days.

Figure 5. ^{11}B MAS NMR spectra and subsequent lineshape fitting of the as-synthesized (a) PB0, (b) PB2-P1, (c) PB2-P3, and (d) PB2-P5 glasses as compared to analogous glass powders recovered from 7 d degradation experiments in Tris-HNO_3 solutions.

Figure 6. (a) ^{11}B{^{1}H} REDOR curves and parabolic fits of the initial dephasing behavior obtained for the unexposed (initial) and exposed (7 d) PB2-P3 glass samples, and the model compound $B(OH)_3$. (b) S_0, S, and ΔS spectra of the exposed glass sample (7 d), obtained by co-adding six spectra from the REDOR curve centered around a dipolar mixing time of 1.07 ms (the 8th point), and simplified spectral deconvolutions highlighting the different dephasing behavior of the boron species represented by the assumed lineshape components. The following lineshape parameters

were used for the deconvolutions: B(III)-a: C_Q = 2.5 MHz, η_Q = 0.5, δ_{cs}^{iso} = 18.2 ppm; B(III)-b: C_Q = 2.7 MHz, η_Q = 0.5, δ_{cs}^{iso} = 13.3 ppm; B(IV)-a,c: Gaussian, δ_{cs}^{iso} = -0.4 ppm, FWHM = 620 Hz; B(IV)-b,c: Gaussian δ_{cs}^{iso} = -1.4 ppm, FWHM = 640 Hz.

Figure 7. ^{31}P MAS NMR spectra for the as-synthesized (a) PB2-P5, (b) MB2-P5, and (c) PA2-P3 samples, as compared to the ^{31}P MAS NMR and ^{1}H→^{31}P CP-MAS NMR spectra of analogous glass powders subjected to 1-, 3-, and 7- day degradation experiments, respectively, in Tris-HNO_3 environments. Lineshape fittings of all the ^{31}P MAS NMR spectra are also displayed. (d) depicts the ^{1}H→^{31}P CP-MAS NMR spectrum of the PB5 1-day sample as analyzed using different ^{1}H→^{31}P contact times.

Figure 8. (a) ^{29}Si MAS NMR and (b) ^{1}H→^{29}Si CP-MAS NMR spectra of selected samples recovered from 14-day experiments in Tris-HNO_3 solutions. Lineshape fittings of ^{29}Si MAS NMR spectra are also displayed in (a).

Figure 9. ERDA spectra of (a) PB2-P5 and (b) MB2-P5 polished glass coupons subjected to 3- and 7- day degradation experiments in Tris-HNO_3 solutions.

Figure 10. SEM images of the cross-section of the PB2-P5 glass subjected to 7-day degradation experiments (taken in secondary electron mode), at (a) 100- and (b) 500-fold magnification. (c) displays the EDS maps of the region depicted in the SEM image of (b).

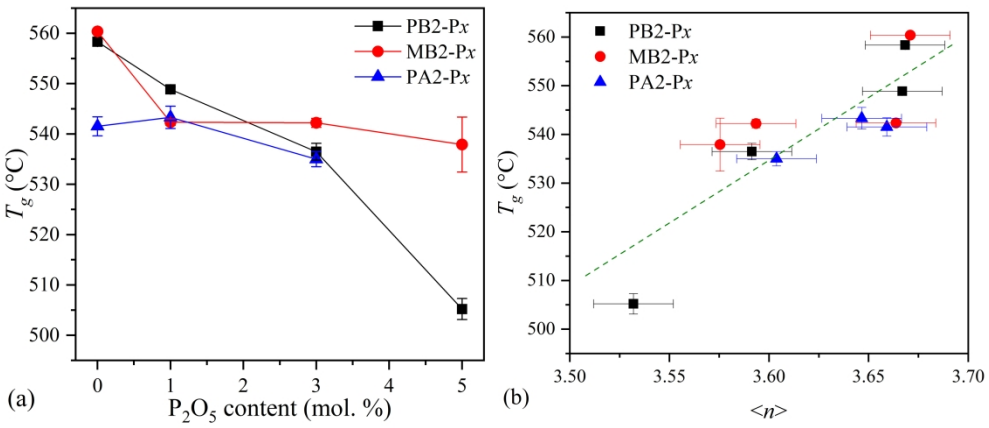

165x71mm (600 x 600 DPI)

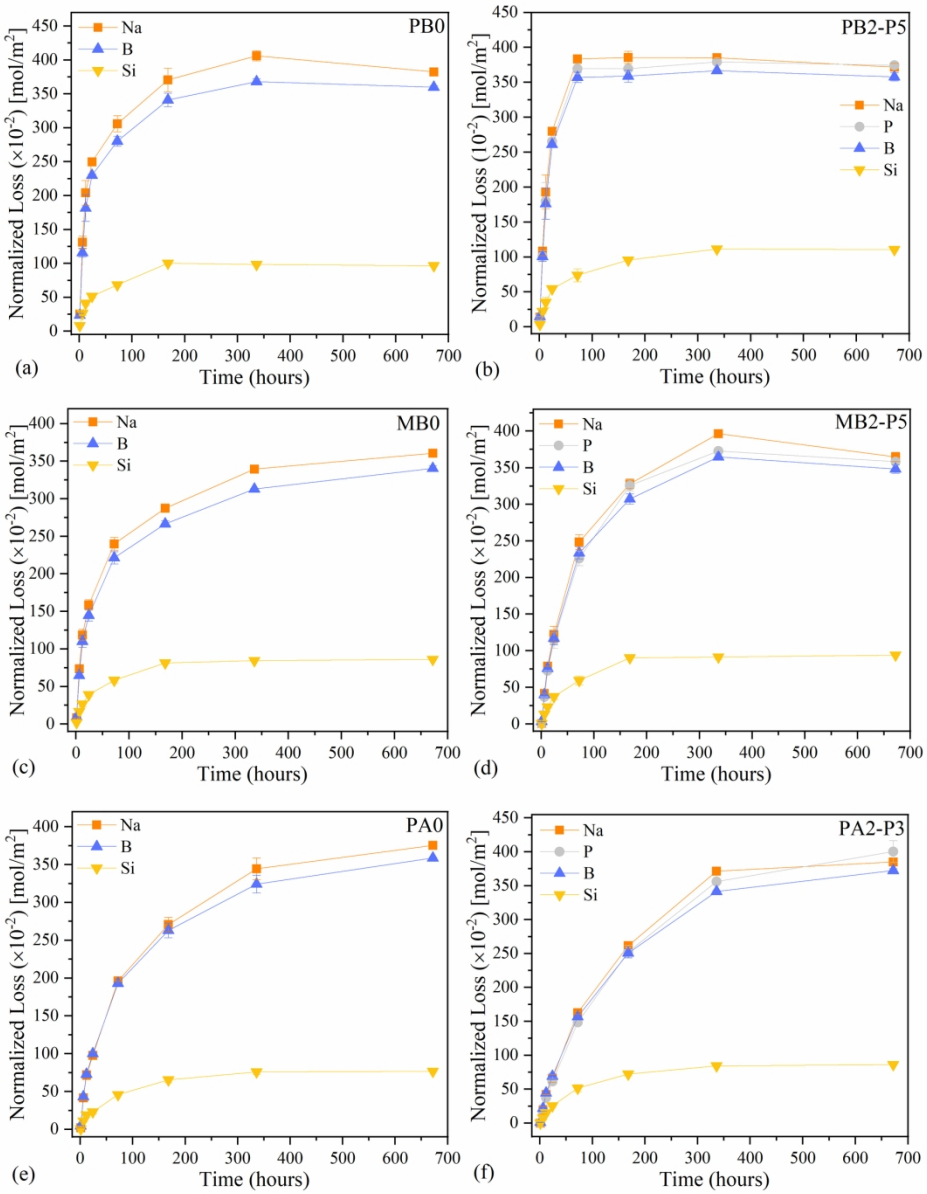

165x210mm (300 x 300 DPI)

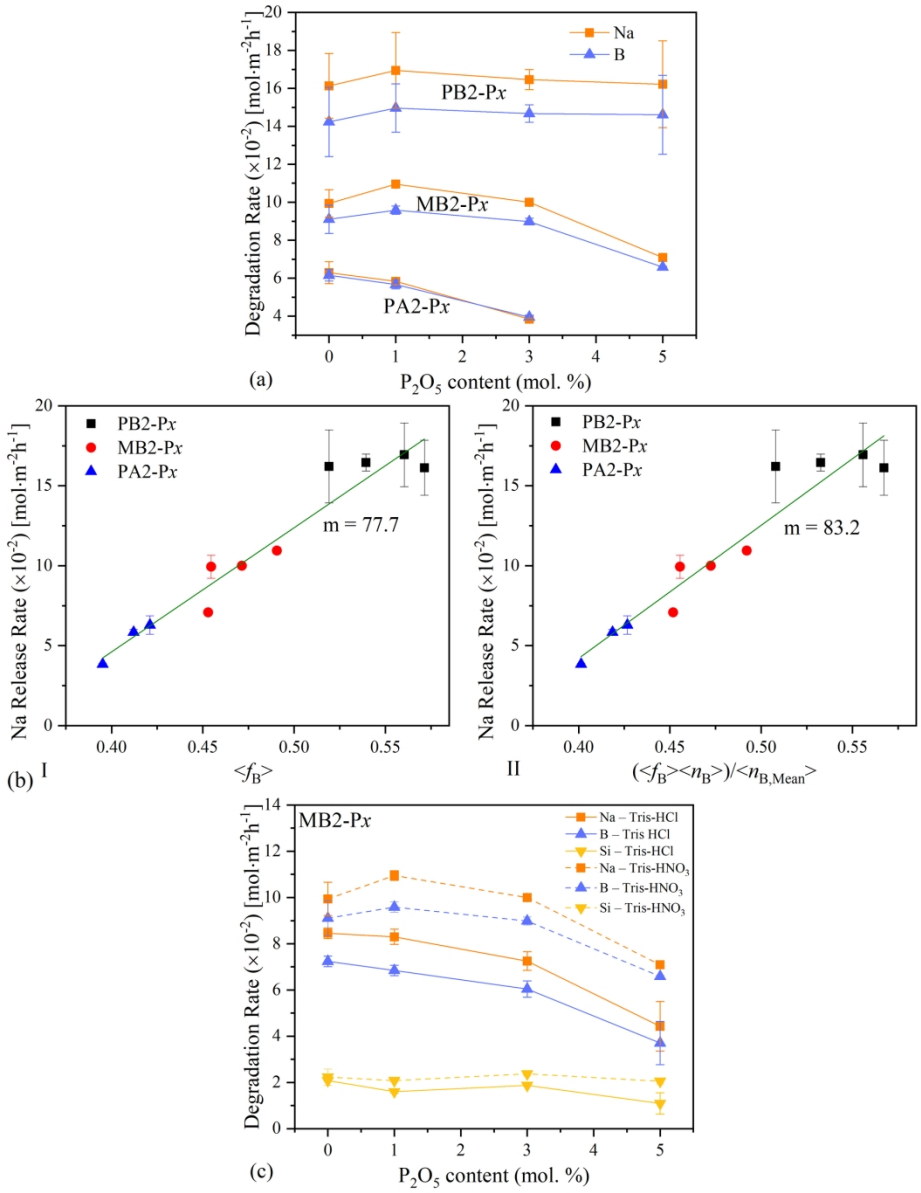

172x220mm (300 x 300 DPI)

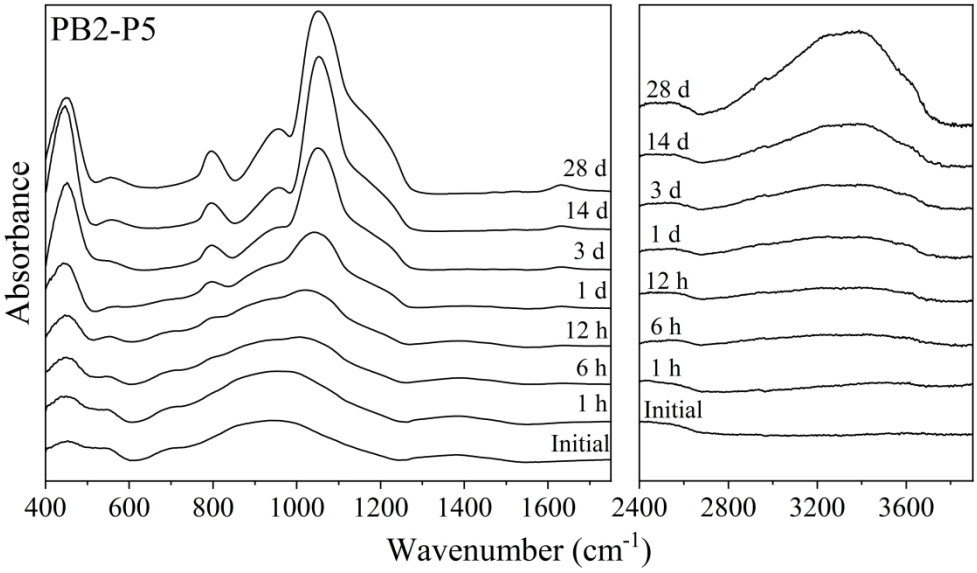

165x97mm (600 x 600 DPI)

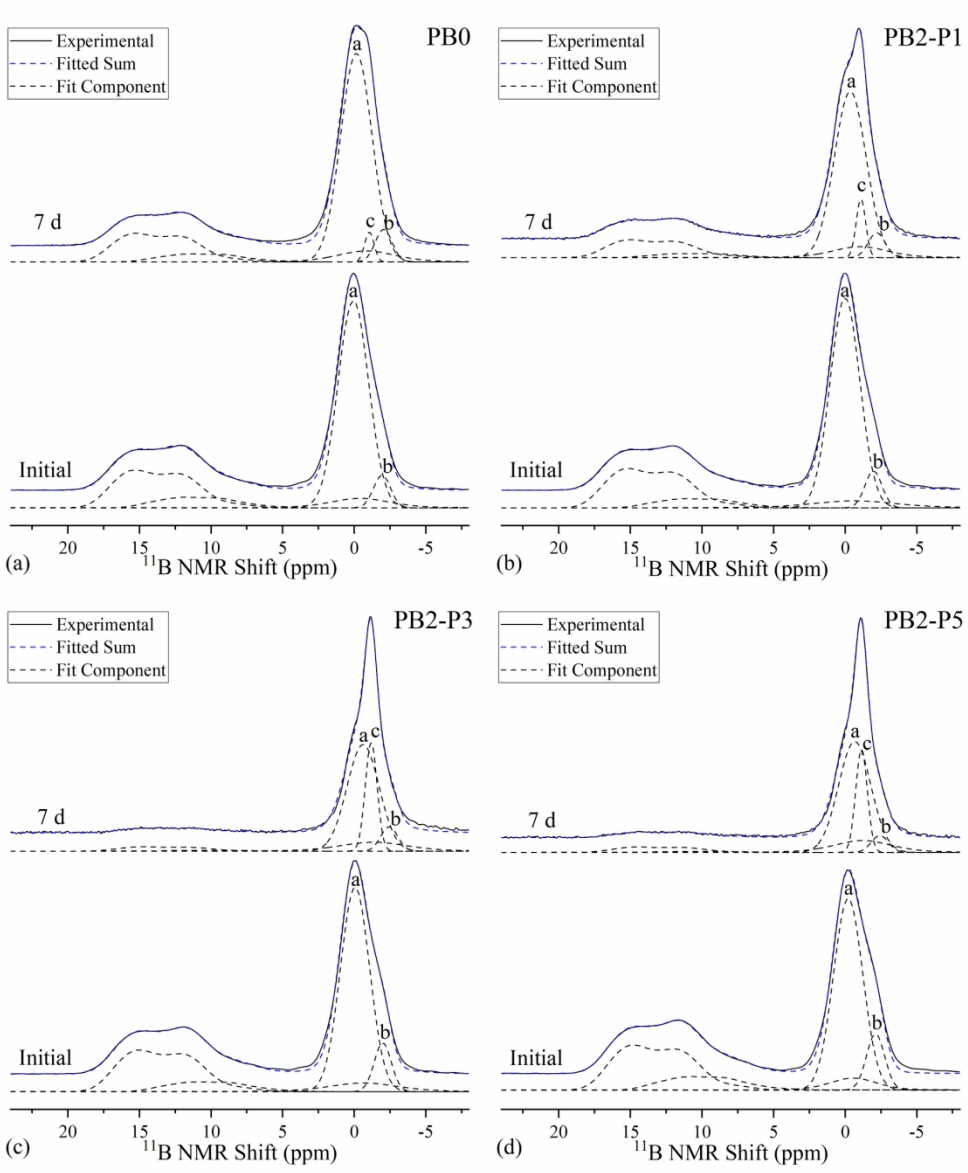

170x203mm (300 x 300 DPI)

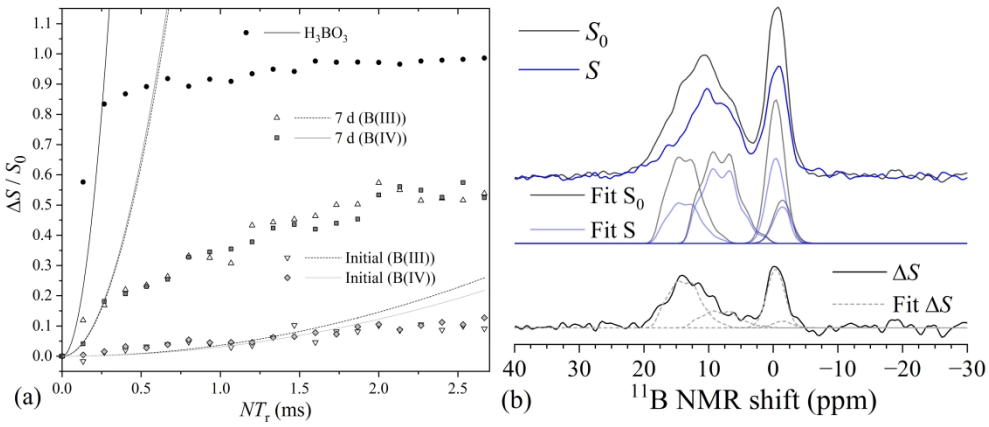

172x76mm (600 x 600 DPI)

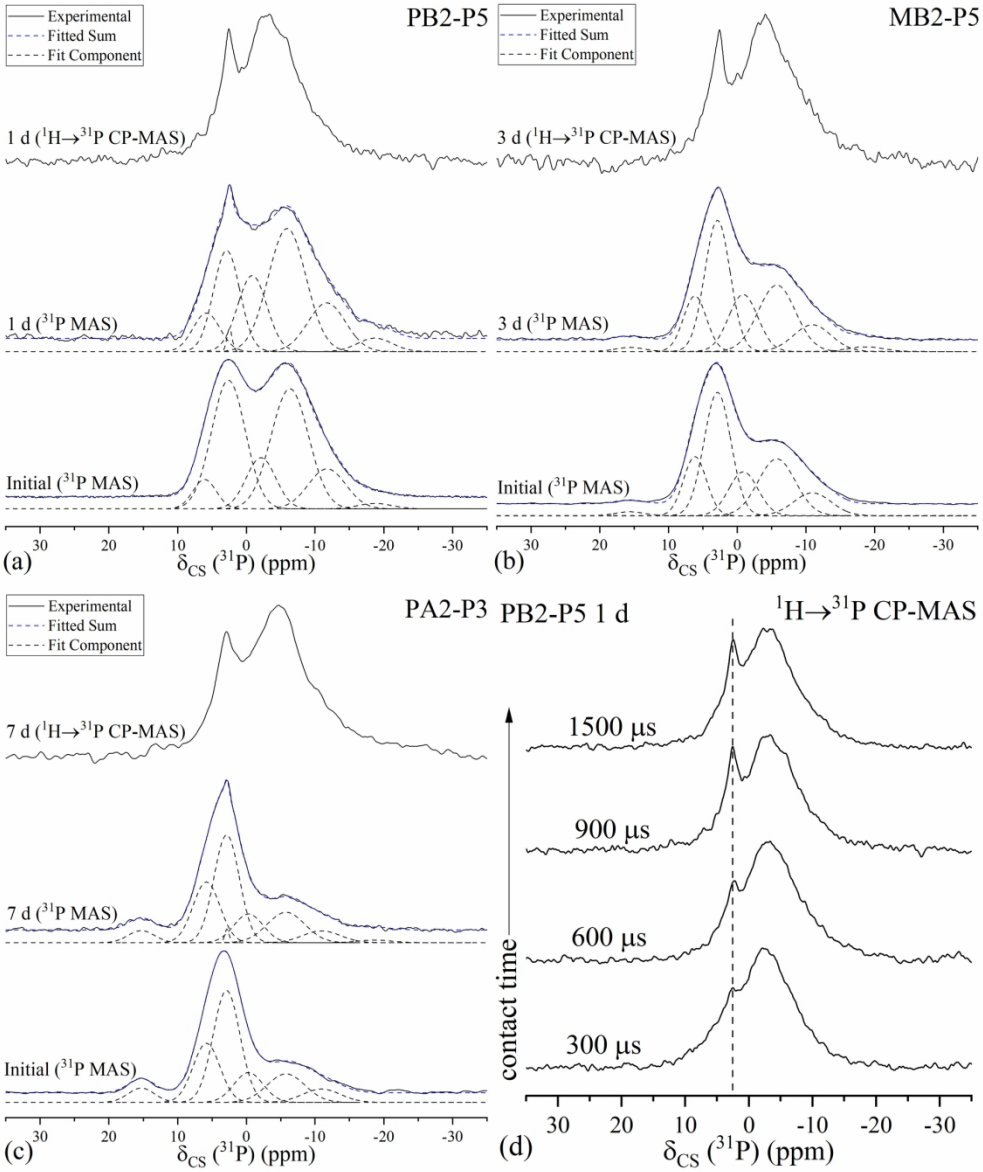

165x196mm (300 x 300 DPI)

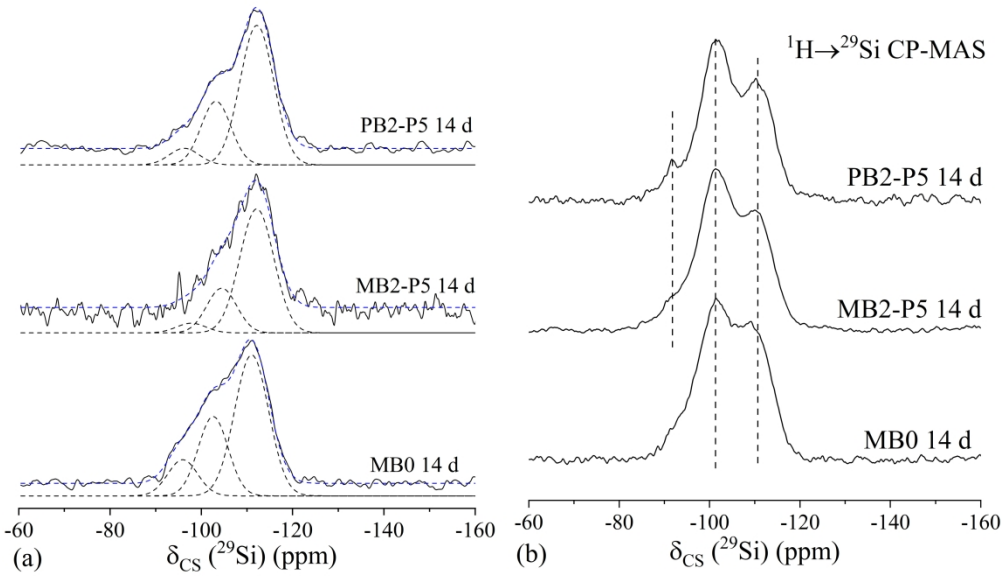

165x96mm (600 x 600 DPI)

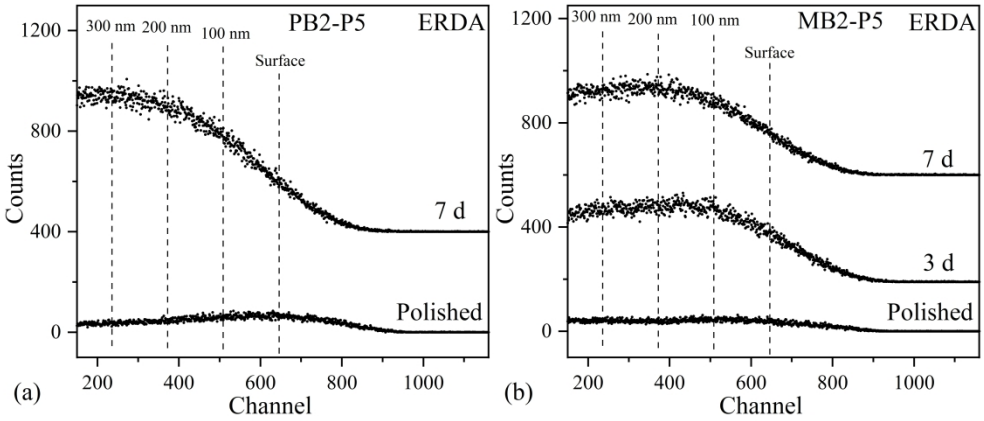

172x76mm (600 x 600 DPI)

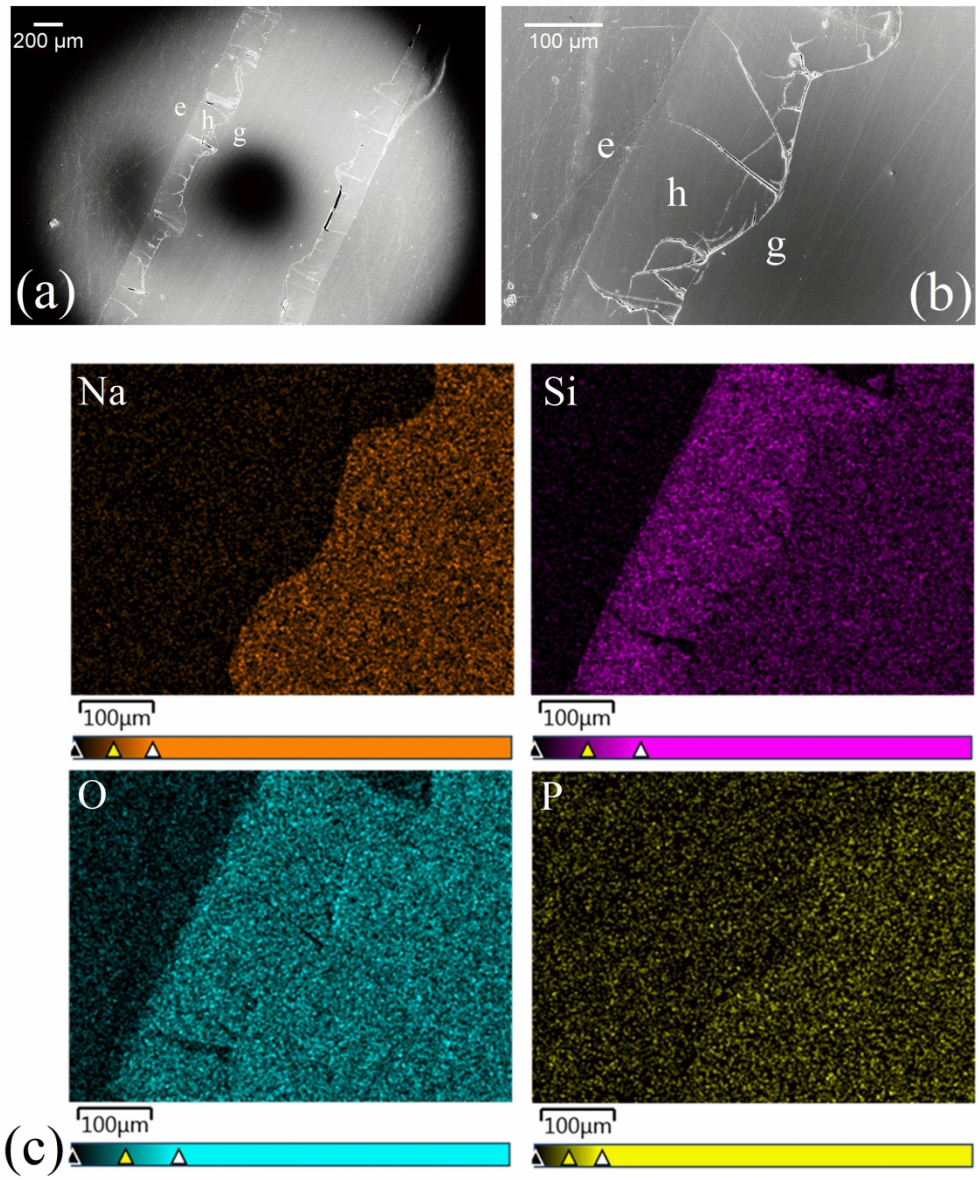

254x304mm (300 x 300 DPI)